

**TECHNISCHE
UNIVERSITÄT
DRESDEN**

Analysis of Material Composition for Range Verification in Proton Therapy

Master-Arbeit
zur Erlangung des Hochschulgrades
Master of Science
im Master-Studiengang Physik

vorgelegt von

Marius Walther
geboren am 19.04.1993 in Friedrichroda

Institut für Kern- und Teilchenphysik
Fakultät Physik
Bereich Mathematik und Naturwissenschaften
Technische Universität Dresden
2019

Eingereicht am 01. März 2019

1. Gutachter: Prof. Dr. Arno Straessner
2. Gutachter: Prof. Dr. Wolfgang Enghardt

Abstract

The presented master thesis tests two different methods to determine the elementary composition of different targets in proton therapy. For verification of the methods, time-resolved prompt gamma spectra which are generated with the simulation toolkit Geant4 are used. In order to determine the usability of the simulation for a proof of principle, the results are compared with experimental data.

While the first method uses cross sections to determine two of the three most frequent elements in the human body, carbon and oxygen, the second works with various statistical analyses. By means of so-called templates, the correct sequencing of the different materials in the target is determined by comparison between the original energy-time spectrum of the target and the combination of multiple spectra of these templates.

Both methods show promising results and could lead to new ways to determine the material composition of an unknown target with the aid of prompt gammas and thus identify the penetration depth of the protons used in the therapy. For this, however, it is necessary to further improve the accuracy of the methods and take into account previously neglected time resolutions of the detectors and time structures of the proton bunches.

Kurzdarstellung

Die vorliegende Masterarbeit testet zwei verschiedene Methoden auf ihre Tauglichkeit zur Bestimmung der elementaren Zusammensetzung verschiedener Targets in der Protonentherapie. Zur Überprüfung der Methoden werden zeitaufgelöste Prompt-Gamma-Spektren genutzt, welche mit dem Simulationsprogramm Geant4 generiert werden. Um die Verwendbarkeit der Simulation als Vergleich zur Realität zu gewährleisten, wird diese zuvor mit experimentellen Daten verglichen.

Während die erste Methode mit Hilfe von Wirkungsquerschnitten zwei der drei häufigsten Elemente im menschlichen Körper, Kohlenstoff und Sauerstoff, bestimmt, arbeitet die zweite mit verschiedenen statistischen Analysen. Mit Hilfe von sogenannten Templates wird die korrekte Aneinanderreihung von verschiedenen Materialien im Target bestimmt, indem das Energie-Zeit-Spektrum des Targets mit dem kombinierten Spektrum dieser Templates verglichen wird.

Beide Methoden zeigen vielversprechende Ergebnisse und könnten neue Wege aufzeigen, die materielle Zusammensetzung eines unbekanntes Targets mit Hilfe von prompten Gammas und somit die Eindringtiefe der verwendeten Protonen zu bestimmen. Dafür ist es jedoch nötig, die Genauigkeit der Methoden weiter zu verbessern und die bis dahin vernachlässigte Zeitauflösung der Detektoren und Zeitstrukturen der Protonen-Bunches zu berücksichtigen.

Contents

1	Introduction	5
2	Physical Background and Basics of Proton Therapy	7
2.1	Protons in Matter	7
2.2	Protons in Radiotherapy	9
2.3	Prompt Gamma-Rays	11
2.3.1	Prompt Gamma-Ray Spectra	13
2.4	Methods for Range Verification in Proton Therapy	16
3	Simulation with Geant4	19
3.1	The Simulation Toolkit Geant4	19
3.2	Physics Lists	19
3.3	Setup of the Simulation Geometry	20
3.4	Comparison between Simulation and Experiment	21
3.4.1	Comparison of the Energy Spectra	22
3.4.2	Comparison of the Energy-Time Spectra	24
4	Methods to Analyse the Prompt Gamma-Ray Spectra	27
4.1	Peak and Energy Region Analysis	27
4.2	Chi-Square Test	29
5	Linearity Method	31
5.1	Angular Distribution of the Simulation	31
5.2	Description of the Method	33
5.3	Linear Correlation between the 6.129 MeV Peak and the Oxygen Amount	37
5.4	Analysis of a Target	39
5.5	Summary and Discussion	41
6	Template Method	42
6.1	Description of the Method	42
6.2	Construction of the Template Database	43
6.3	Description of the Applied Test	44
6.4	Test with 3 cm long Targets	47
6.5	Influence of the Bragg Peak	56
6.6	Statistical Benchmarking	60
6.7	Summary and Discussion	64
7	Conclusion and Outlook	65
8	References	69

1 Introduction

Due to advanced medical knowledge in Western civilisations and thereby increasing life expectancy, cancer has become a more and more dominant cause of death. Further reasons for that are growth of population as well as types of cancer that are connected to modern lifestyle. The World Health Organization (WHO) predicts that new cases of cancer will rise up to 25 million per year until 2030 [1]. In 2018, the global cancer burden is estimated to be 18.1 million new cases and 9.6 million deaths [2]. This makes cancer the second most frequent cause of death in countries like Germany. Cancer treatment is therefore one of the most important research fields in contemporary medicine. Because of the possibilities opened up by radiotherapy, like X-ray and proton therapy, physics and medicine work together on further improving these methods. The usage of particles – especially protons – as an effective method of treatment was first suggested by ROBERT R. WILSON in 1949 [3]. Since then, particle therapy has come a long way. Today more than 80 facilities are operating it worldwide and more are under construction [4, 5]. More than 100 000 patients were treated as of 2015 [6].

Protons have the feature to deposit most of their energy at a predictable depth inside a target. That makes them work well for tumor treatment. Although the penetration depth can be determined, it is subject to fluctuations and uncertainties. For one thing, the calculated ranges only represent a mean value. Further, uncertainties arise when determining the energy loss of the protons in the target. The penetration depth is also influenced by changes in the patient's body. In Order to maximise the potential of proton therapy, these range uncertainties need to be eliminated. The most preferable way is to use only information that originate from the radiation itself during the treatment. These so-called in vivo range verification methods can determine the penetration depth of the protons in real time. Currently, different methods are under development and are tested based on various secondary signatures that encode the range of the protons. One of the most promising tool to do so are prompt gamma-rays. These photons are created by the interaction of the proton with the target in picoseconds or less. By detecting and analysing their time and energy distribution, conclusions about the interacting proton and therefore about the target can be made.

Moreover, methods based on the use of collimators in the form of slits are under development. This enables researchers to obtain information about the location of the reaction and link the results to a specific depth in the target. This collimation also leads to a selection of photons and thereby to a decreasing number of detected prompt gammas. In order to prevent this as well as to decrease the expenses and increase the flexibility, a detection of all prompt gammas without collimation is proposed. One way to determine the penetration depth of protons with such a system could be to determine the material composition of the whole target. By doing this,

the energy loss of the proton for each part of the target could be computed and with that the penetration depth could be calculated. This also reveals the deposit dose inside the patient.

The objective of this thesis is to present and test methods for determining the material composition along the proton path and to give an initial assessment of whether further investigations in these methods are worthwhile. For this purpose, spectra of prompt gamma-rays are generated with a simulation program and analysed and compared with the aid of various methods. At first a general overview on proton radiotherapy is given in Chapter 2. This chapter covers basics of proton physics in matter and currently studied methods for range verification. In Chapter 3, the simulation program Geant4, that is used in this thesis, is introduced and the simulations are compared to experimental results. Furthermore, the specific setup is motivated and explained. Chapter 4 deals with the different methods that are used for the analysis and comparison of the generated spectra. In Chapters 5 and 6 the two explored methods are described and tested. The first one uses a linear correlation between one of the prompt gamma peaks and the oxygen amount inside the target as a starting point to determine the target composition. The second method relies on the usage of so-called templates to reconstruct a larger unknown target out of smaller target slices. For this method a statistical benchmarking is also given in the chapter. In Chapter 7 the findings of this thesis are summarised and an outlook is presented on possible ways to improve the described methods. Remaining problems that need to be solved in order to bring these methods closer to medical practise will be addressed as well.

2 Physical Background and Basics of Proton Therapy

Developing new methods of range verification requires profound knowledge of proton therapy and currently investigated methods, and about possible signatures and their properties originating from the interaction between the proton and the target. As proton therapy is a field of huge interest and the different aspects of this field could fill books, this chapter only covers the basics of proton therapy and focuses on the aspects that are necessary for understanding the proposed solution for range verification in this thesis. First of all, a short introduction to the behaviour of protons in matter is given. Subsequently, the usage of protons in radiotherapy and their advantages and disadvantages are explained. As a possible solution for the given disadvantages prompt gamma-rays are then presented and their properties described. Finally, different methods that are currently used in the field of proton therapy are explained briefly.

2.1 Protons in Matter

While the proton moves through the target the main interaction comes through Coulomb force. The positively charged proton interacts with the orbital electrons of the material. In rare cases the proton can scatter inelastically with the nuclei and thereby excite the nucleus. These processes lead to an energy loss of the proton and eventually to a stop of the particle inside the material. This process can be described by the linear stopping power

$$S = - \left(\frac{dE}{dx} \right).$$

S is a representation of the energy loss dE after a certain distance dx inside a target. The stopping power by ionisations can be calculated by the **Bethe formula** [7] with the corrections of BARKAS [8] and BLOCH [9]:

$$- \left(\frac{dE}{dx} \right) = 2\pi N_a r_e c^2 \rho z_{\text{eff}} \frac{Z}{A} \frac{1}{\beta^2} \left[\ln \frac{2m_e c^2 \beta^2 \gamma^2 T_{\text{max}}}{I^2} - 2\beta^2 - \delta - 2\frac{C}{Z} \right]. \quad (1)$$

β and γ are the known expressions

$$\beta = \frac{v}{c}$$

and

$$\gamma = \frac{1}{\sqrt{1 - \beta^2}}.$$

N_a is AVOGADROS number, r_e the classical electron radius, m_e represents the rest mass of the electron and e its charge. The charge of the incident particle is given by z_{eff} . δ is the correction for the density and C for the shell. T_{max} describes the maximum energy that can be transferred in a single collision. The important part is the influence of different materials on the formula, namely the density ρ , the average excitation potential of the target atom I and the mass number A as well as the charge Z of the nuclei.

The interaction of the proton with the target leads to a specific curve of the deposit energy and therefore of the deposit dose, called the **Bragg curve** with the typical **Bragg peak** [10, 11]. Along its path the proton deposits only a relatively small amount of energy. Shortly before it comes to rest, most of the energy is deposited inside the small area of the peak. This can be explained with the Bethe-Bloch formula: the stopping power has a $1/v^2$ dependency, so the energy loss increases with the slowing down of the particle. It is also important to note that the calculated energy loss is a mean value and that the slowing down process of protons in matter is subject to fluctuations. As the stopping process is a stochastic one, the Bragg curve is broadened (as shown in Figure 1).

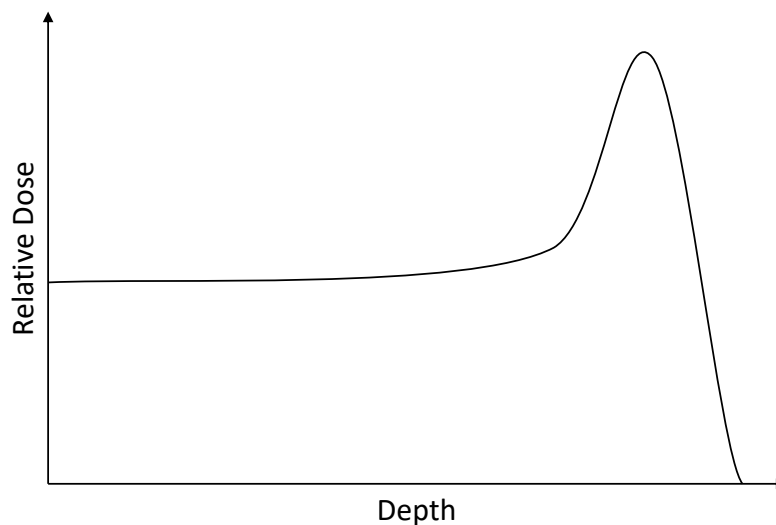


Figure 1: Typical shape of the broadened Bragg curve with a Bragg peak.

The penetration depth of one specific particle cannot be exactly determined. Instead a mean range $R(E_0)$ can be calculated by integrating the reciprocal stopping power over energy. That gives the so-called **continuous slowing down approximation** (CSDA):

$$R(E_0) = \int_0^{E_0} \frac{1}{S(E_0)} dE.$$

For this approximation energy-loss fluctuations are neglected. Typical penetration

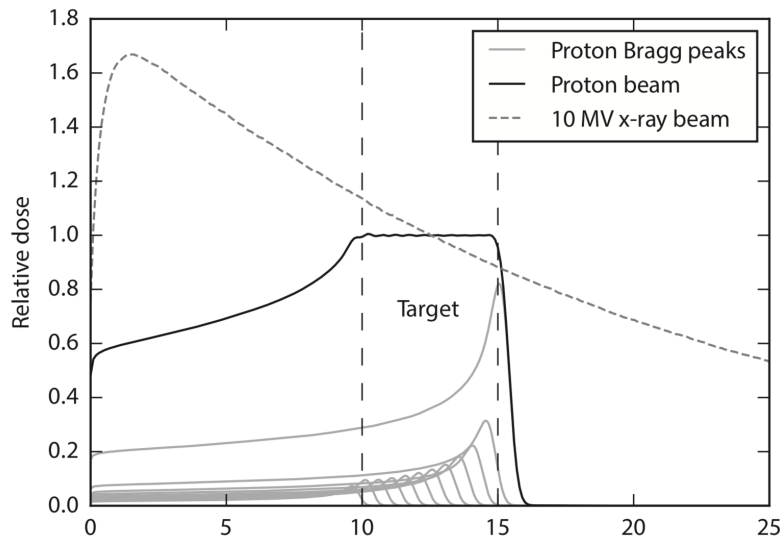


Figure 2: Depth-dose distribution of an X-ray beam and multiple proton beams with the resulting spread out Bragg peak in water. (Taken from [13])

depths are in the range of centimetres. For a proton energy of 130 MeV the penetration depth in water is 12.26 cm and in carbon 6.89 cm. The values are calculated with the PSTAR and ASTAR Databases for Protons and Helium Ions from the National Institute of Standards and Technology (NIST) [12].

2.2 Protons in Radiotherapy

The behaviour of the proton leads to possible advantages of proton therapy over other radiotherapies, like X-ray therapy. Photon beams have an exponential dose distribution and therefore deposit less dose by Compton scattering in larger depths of the target as more photons are removed from the beam. In order to deposit a higher dose at the tumor compared to the surrounding tissue or organs, several photon beams from different directions have to be used. Proton therapy, on the other hand, works with a fixed beam direction. In order to deposit the correct dosage amount, the energy of the proton beams is varied, thereby changing the penetration depth. The resulting total radiation dose of the multiple proton beams is called the **spread-out Bragg peak (SOBP)**. The depth-dose distribution of the two particles can be seen in Figure 2. Compared to X-ray therapy, tissue behind the tumor can be spared and tissue in front of the tumor receives a weaker dose.

Accelerators like a isochronous cyclotron are used to bring the protons to the required energy. A degrader is used to reduce the energy of the protons because the accelerator only delivers the proton bunches with a fixed energy. Another important factor is that protons have a bunch structure which results from "the phase-focusing

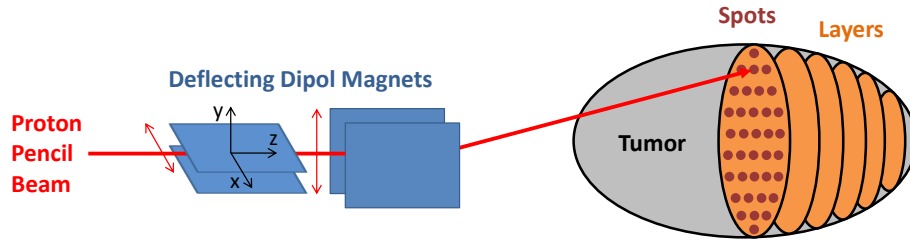


Figure 3: Schematic representation of the Pencil-Beam-Scanning-Mode. The proton beam is deflected by the magnets in the x- and y-direction and the energy of the beam modulates the depth in z-direction. By this the whole tumor is scanned point by point. (Taken from [16] with courtesy of Jonathan Berthold)

periodic acceleration of protons in the resonator gaps of an isochronous cyclotron" [14]. These bunches leave the cyclotron at the frequency of the accelerating high voltage. The bunches themselves already have a time width in their internal time structure in reference to the frequency of the accelerator. This bunch time spread is further increased by the degrader [15]. Low proton energies can therefore lead to a higher time uncertainty as the particles need to cross more matter from the degrader. This in turn has an influence on range determination methods working with the time information of the protons.

There are two ways to deliver the proton beam to the patient: Double-Scattering and Pencil-Beam-Scanning-Mode. In Double-Scattering-Mode the proton beam is passively modulated and collimated. Scatterers broaden the beam which has a fixed energy. Then a modulator wheel and a range compensator slow down the beam so that the correct dose is deposited in the entire tumor. In Pencil-Beam-Scanning-Mode, the target is divided into several isoenergetic layers which are further divided into so-called spots. By using deflecting dipole magnets, the beam is deflected to scan the target spot by spot (see Figure 3). By changing the beam energy, the different layers can be reached. Pencil-Beam-Scanning is the widely accepted method in proton therapy as it has the advantage of being flexible. Instead of creating a new range compensator for each patient and each tumor, the same setup can be used again each time. The methods described later in this thesis are designed for Pencil-Beam-Scanning-Mode. The simulations used in this thesis work with a fixed beam energy and describe the irradiation of one pencil beam spot.

A major problem proton therapy is currently facing is the influence of range uncertainties on the treatment plan. Before the treatment can be started, a computed tomography scan (CT) is made. With the hereby collected data and the knowledge of the stopping power of different materials, the treatment plan can then be created. This way the required energy for the proton beams is calculated. With the conversion

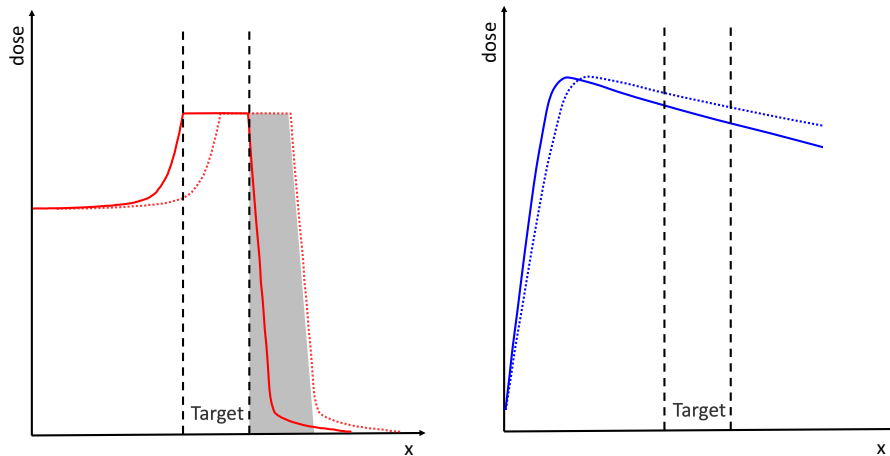


Figure 4: Effect of range uncertainties on the deposit dose inside the human body for proton therapy with a SOBP (left) and for photon therapy with an X-ray beam (right).

of CT Hounsfield units into relative stopping power, range uncertainties of the proton inside the target arise. Additional patient positioning, movements during the treatment and anatomical changes after the CT also contribute to these uncertainties [17].

In X-ray therapy, these range uncertainties have only a small effect on the delivered dose, whereas in proton therapy, they lead to a shift of the Bragg peak and therefore to a change of the position of the deposit energy and dose. The changed dose deposition for an X-ray and an SOBP is illustrated in Figure 4.

To ensure that the complete tumor is covered, robust safety margins are used. For example the margin used in the "Universitäts Protonen Therapie Dresden" (UPTD) is 3.5 % of the proton range plus 1 mm [18]. These margins, however, prevent proton therapy from reaching its full potential as they lead to damage to the surrounding tissue and organs. Therefore current research focuses on a way to tackle this problem and find ways to verify the range of proton beams during a treatment. One promising way is the usage of so-called prompt gamma-rays which are produced along the path of the proton.

2.3 Prompt Gamma-Rays

Prompt gamma-rays are produced by proton-nuclear interactions. The prompt gammas are the result of the de-excitation of the excited nuclei. This reaction takes less than 1 ns which is why they are called prompt gamma-rays. An example for such a reaction can be seen in Figure 5.

Because most of the photons have energies up to 7 MeV or higher [19] they can

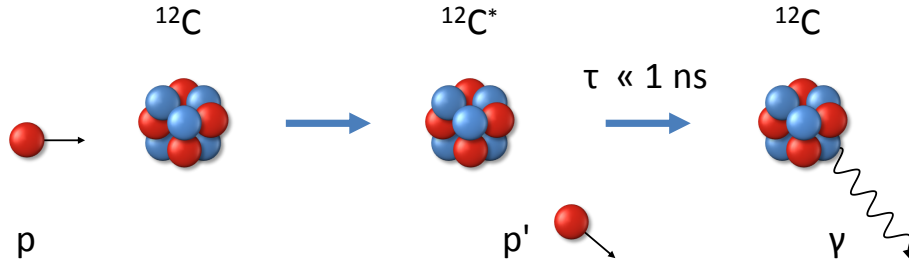


Figure 5: Inelastic reaction between a proton and a carbon ¹²C nucleus leading to the production of a prompt gamma-ray. (Taken from [16] with courtesy of Jonathan Berthold)

leave the patient with a high probability. The intensity reduction is defined by the **Beer-Lambert law**:

$$I = I_0 e^{-(\mu/\rho_m)\rho_m l}$$

with the initial intensity I_0 , the attenuation coefficient μ , the mass density ρ_m and the length l of the attenuation. The mass attenuation coefficient μ/ρ_m for water and a photon energy of 1 MeV is $7.072 \cdot 10^{-2} \text{ cm}^2/\text{g}$. This results in a loss of 29.78 % of the initial intensity for an attenuation length of 5 cm. For a photon energy of 8 MeV this loss is reduced to 11.44 % with a coefficient of $2.429 \cdot 10^{-2} \text{ cm}^2/\text{g}$ [20]. For these energies the dominant interactions are Compton scattering and pair production [21]. Figure 6 shows a comparison between the depth dose distribution of a proton beam and the total number of gammas that are emitted from the target. As can be seen, the number of gammas rises slightly with the penetration depth of the proton and reaches its maximum short before the Bragg peak.

The cross sections of the reactions are energy-dependent, so that different gamma spectra result of different proton energies. These spectra can therefore be used to draw conclusions about the energy and penetration depth of the protons used. Since the frequency of the reaction also changes with the composition of the target, statements about this can also be made.

Another important point is the angular dependency of the reaction cross section, as it is important to know where to locate the detector to the target and if the angle influences the frequency of the reactions. As stated in [23], the cross sections are obtained by assuming that the angular gamma emission can be described with Legendre polynomials [24]. Similar results are presented in [25]. It is important to note that the angular dependency can be disturbed or smeared by the collision kinematics. In [26] and [27] it is stated that the emission of prompt gammas is isotropic. In [28] it is observed that the ¹²C($p, p\gamma_{4.44 \text{ MeV}}$)C reaction has a larger differential cross section when the detector is moved away from the 90° position, but

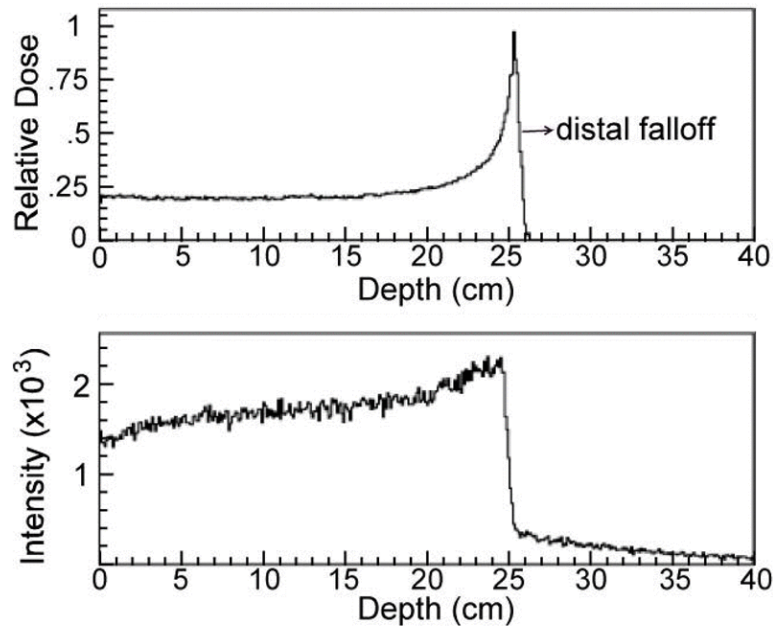


Figure 6: Depth dose distribution of a proton beam in a water target with an energy of 200 MeV and the corresponding total number of gammas emitted. (Adopted from [22])

all other processes for this energy are isotropic. For a clear statement regarding the simulation that is used in this thesis, an analysis is made in Section 5.1 to see if the cross sections used in calculations need to be adjusted depending on the angle between the target and the detector.

2.3.1 Prompt Gamma-Ray Spectra

The human body mainly consists of three elements: hydrogen, oxygen and carbon. For the analysis of prompt gamma-rays the de-excitation lines originating from these elements are most important. Table 1 contains most of the interesting transitions for this thesis.

For testing range verification methods before they are applied in a clinical environment, targets made out of water or poly(methyl methacrylate) (PMMA) are used as they show similar behaviour to human tissue with regard to elemental composition and stopping power. PMMA is a transparent thermoplastic with the chemical formula $C_5O_2H_8$ and has a density of 1.18 g/cm^3 . An example of a prompt gamma-ray energy spectrum from PMMA (hereafter referred to as energy spectrum) with the important lines from Table 1 can be seen in Figure 7. As one can see some of the peaks with their respective single and double escape peaks are clearly visible. These escape lines are a result of the interaction between the photon and the detector material via pair

Table 1: Some important gamma-ray lines from proton reactions with ^{16}O and ^{12}C [29].

Energy [MeV]	Transition	Nuclear Reaction	Mean life [s]
0.718	$^{10}\text{B}^{*0.718} \rightarrow \text{g.s.}$	$^{12}\text{C}(\text{p}, \text{x})^{10}\text{B}^*$	$1.0 \cdot 10^{-9}$
1.022	$^{10}\text{B}^{*1.740} \rightarrow ^{10}\text{B}^{*0.718}$	$^{12}\text{C}(\text{p}, \text{x})^{10}\text{B}^*$	$7.5 \cdot 10^{-15}$
		$^{16}\text{O}(\text{p}, \text{x})^{10}\text{B}^*$	$7.5 \cdot 10^{-15}$
2.000	$^{11}\text{C}^{*2.000} \rightarrow \text{g.s.}$	$^{12}\text{C}(\text{p}, \text{x})^{11}\text{C}^*$	$1.0 \cdot 10^{-14}$
2.313	$^{14}\text{N}^{*2.313} \rightarrow \text{g.s.}$	$^{16}\text{O}(\text{p}, \text{x})^{14}\text{N}^*$	$9.8 \cdot 10^{-14}$
4.438	$^{12}\text{C}^{*4.439} \rightarrow \text{g.s.}$	$^{12}\text{C}(\text{p}, \text{p}')^{12}\text{C}^*$	$6.1 \cdot 10^{-14}$
		$^{16}\text{O}(\text{p}, \text{x})^{12}\text{C}^*$	$6.1 \cdot 10^{-14}$
4.444	$^{11}\text{B}^{*4.445} \rightarrow \text{g.s.}$	$^{12}\text{C}(\text{p}, 2\text{p})^{11}\text{B}^*$	$5.6 \cdot 10^{-19}$
5.180	$^{15}\text{O}^{*5.181} \rightarrow \text{g.s.}$	$^{16}\text{O}(\text{p}, \text{x})^{15}\text{O}^*$	$< 4.9 \cdot 10^{-14}$
5.240	$^{15}\text{O}^{*5.241} \rightarrow \text{g.s.}$	$^{16}\text{O}(\text{p}, \text{x})^{15}\text{O}^*$	$3.3 \cdot 10^{-12}$
5.269	$^{15}\text{N}^{*5.270} \rightarrow \text{g.s.}$	$^{16}\text{O}(\text{p}, 2\text{p})^{15}\text{N}^*$	$2.6 \cdot 10^{-12}$
5.298	$^{15}\text{N}^{*5.299} \rightarrow \text{g.s.}$	$^{16}\text{O}(\text{p}, 2\text{p})^{15}\text{N}^*$	$1.2 \cdot 10^{-14}$
6.129	$^{16}\text{O}^{*6.130} \rightarrow \text{g.s.}$	$^{16}\text{O}(\text{p}, \text{p}')^{16}\text{O}^*$	$2.7 \cdot 10^{-11}$
6.175	$^{15}\text{O}^{*6.176} \rightarrow \text{g.s.}$	$^{16}\text{O}(\text{p}, \text{x})^{15}\text{O}^*$	$< 2.3 \cdot 10^{-14}$

production. The resulting positron is captured in the detector material and leads to the creation of two photons of 511 keV each. As one or both of these photons leave the detector, the single and double escape peaks are formed additionally to the full-energy peak. Due to Compton scattering, the Compton continuum and the Compton edge are created. Figure 8 shows a schematic representation of these effects. The sharp edge at the end of the Compton plateau is the Compton edge and represents the highest energy that can be transferred to the electron by the gamma. The plateau itself represents the fact that the photon can be scattered at different angles and therefore deposits different amounts of energy.

Because of the Doppler broadening and the energy resolution of the detector the 4.444 MeV line due to the reaction $^{12}\text{C}(\text{p}, 2\text{p})^{11}\text{B}^*$ and the 4.438 MeV line due to the reactions $^{12}\text{C}(\text{p}, \text{p}')^{12}\text{C}^*$ and $^{16}\text{O}(\text{p}, \text{x})^{12}\text{C}^*$ can not be separated. With lower resolution of the detector the lines around 5.2 MeV cannot be distinguished as one can see in Figure 9.

The effects of low detector resolution and the Doppler broadening as well as the effect of Compton scattering inside the detector lead to an overlap of lines in the energy spectrum. These effects need to be considered in order to determine the correct amount of events for specific lines as they complicate the spectrum.

Next to energy spectra, so-called energy-time spectra can also be measured. These are time-resolved energy spectra. The arrival time of the gammas in the detector

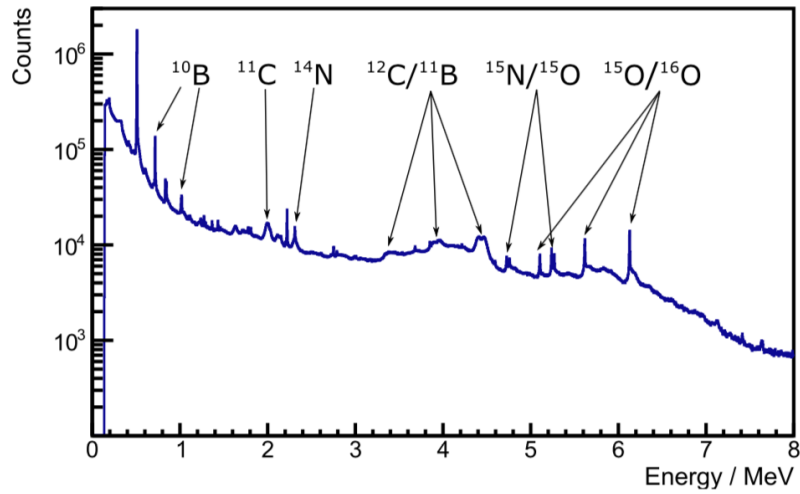


Figure 7: Prompt gamma-ray spectrum of a PMMA target produced by a 150 MeV proton beam. The data was measured with a High-Purity Germanium (HPGe) detector. (Taken from [30])

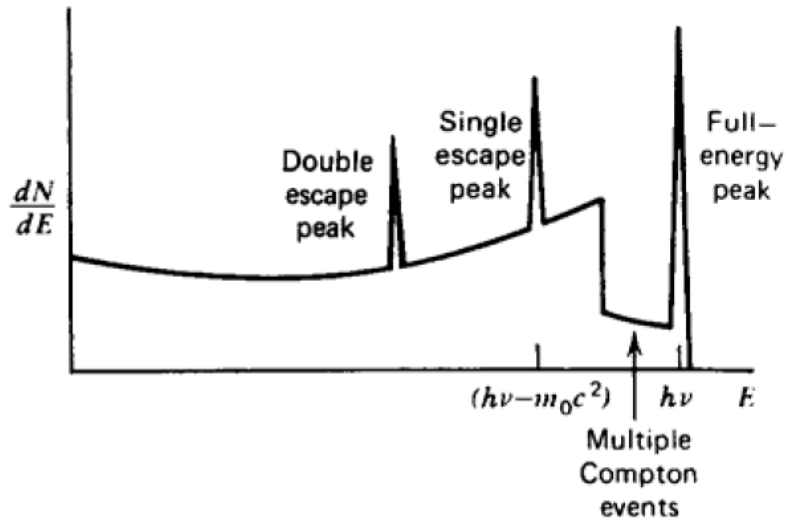


Figure 8: Schematic representation of an energy spectrum of photons with the effects of Compton scattering in a detector. The photon energy is larger than 1.022 MeV. (Taken from [21])

in reference to the time at which the protons leave the accelerator is selected as the reference time in the spectrum. The clock of the cyclotron can be used as a reference time. With the time of prompt gamma production being less than 1 ns and the cycle of the cyclotron larger than a few ns, the time information can be used

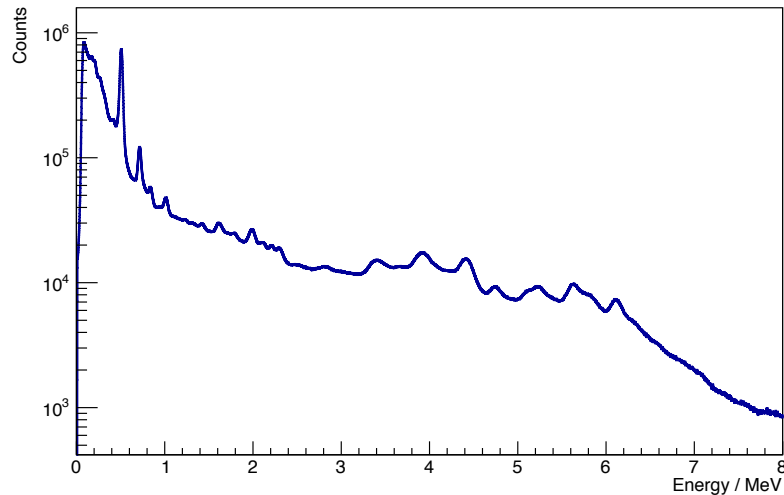


Figure 9: Prompt gamma-ray spectrum of a PMMA target produced by a 224.5 MeV proton beam. The data was measured with a cerium(III) bromide (CeBr_3) detector. (Adopted from [31])

to determine the penetration depth of the proton or identify from where inside the target the gamma comes. In Figure 10 such spectra are visualised for different target materials. The difference resulting from different compositions can clearly be seen. Due to reactions between protons and oxygen nuclei, prompt gammas are present in form of peaks above 5 MeV in the H_2O target whereas in the H_2C target these peaks do not exist. Figure 11 depicts the discrete gamma-ray lines over the penetration depth in these targets. Again the correlation with the Bragg peak can be seen. In the following section the usage of these different information and properties of the spectra in proton therapy is described.

2.4 Methods for Range Verification in Proton Therapy

Additionally to methods that are based on prompt gamma detection, other methods are being used for range verification. For example the usage of positron emission tomography [32–34] or acoustic signatures [35, 36] of the proton beam. As in this thesis the focus lies on range verification with the aid of prompt gamma-rays, alternative methods will not be introduced here.

For range verification with prompt gamma-rays different aspects of the detected photons are used. The strong spatial correlation between the gamma emissions and the dose deposition [37, 38] is used by prompt gamma-ray imaging (PGI). Different prompt gamma camera systems using passive collimation in form of a slit or a hole are used to detect one-dimensional spatially resolved prompt-gamma spectra. Prompt gamma spectroscopy (PGS) makes use of the fact that the emission spectrum

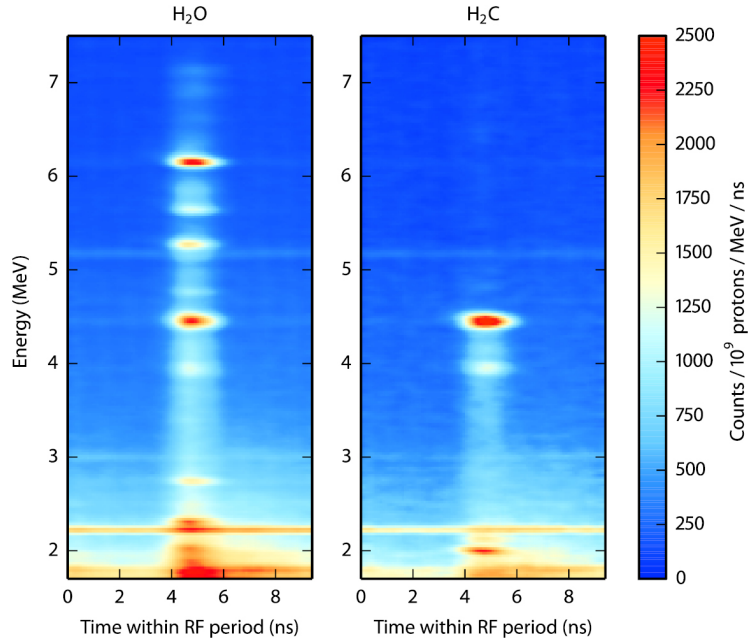


Figure 10: Comparison between energy-time spectra of two different targets H_2O (left) and H_2C (right) that were produced by a 165 MeV proton beam. (Taken from [23])

depends on the energy and therefore on the penetration depth of the protons [23]. This is achieved by analysing the ratios of prominent peaks in the measured energy spectrum and thereby the energy dependency of the individual cross-sections. The time the particle needs to cross the target, also referred to as transit time, is used by prompt gamma-ray timing (PGT) [39]. This time is influenced by the properties of the material. A higher stopping power deriving from a higher density of the material leads to a shorter range in the target and thus to a shorter transition time. These effects on the spectra are measured and analysed.

In this thesis a system without a collimator is used as well as the benefits of PGT and PGS. The spectra, as shown in Figure 10, are simulated and analysed. Chapter 5 explores a method which correlates the timing information to the place of the reaction and then uses PGS to determine the material composition of the target. The method in Chapter 6 uses the whole energy-time spectrum to determine the composition of the target. In the next Chapter the simulation setup is described and the results of the simulations are compared to experimental data.

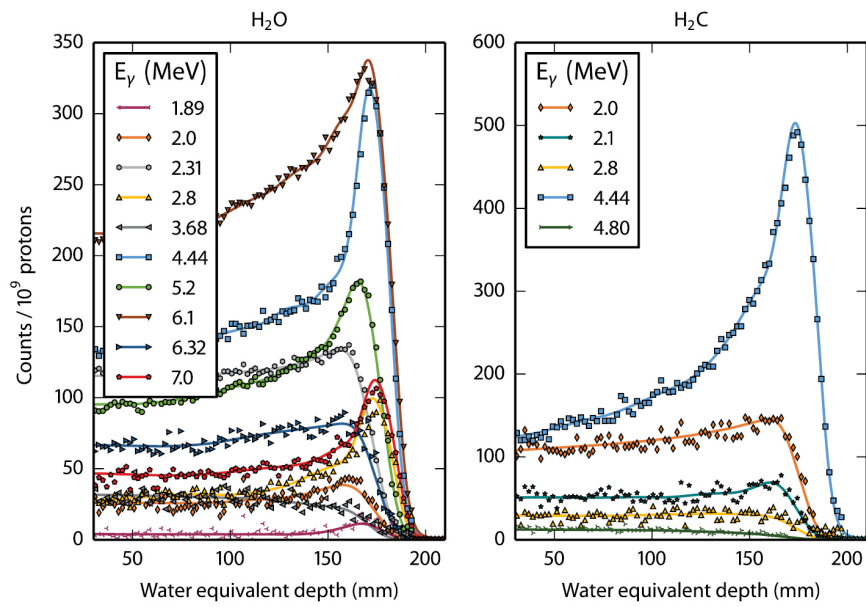


Figure 11: Comparison between discrete prompt gamma-ray lines of two different targets H_2O (left) and H_2C (right) that were produced by a 165 MeV proton beam. (Taken from [23])

3 Simulation with Geant4

For testing different methods to determine the composition of targets, Monte Carlo simulations can be chosen as a cheap and controllable way to generate the needed data sets. The goal of the simulation is to generate energy-time spectra of different materials with varying proton energies. Most importantly the simulation should represent experimental results in such a way that the investigated methods could also be applied to real spectra. For this purpose, the general trend of the simulation should match the results of experimental measurements. Geant4 is selected as the simulation program because it is suitable and already in use for investigations in the field of radiotherapy. Therefore this chapter introduces Geant4 and gives a brief explanation of its functionality. In this context, a short discussion of physics lists is included as they are responsible for the representation of the spectra. Subsequently the simulated setup of the geometry is described. In the last section some of the simulated spectra are shown and compared to experimental data. Thereby the suitability of the simulation for a proof of principle of different range verification methods is examined.

3.1 The Simulation Toolkit Geant4

The Geant4 toolkit has been created for the purpose of simulating particles passage through different materials with the possibility to change the geometry of detectors and targets. The name stands for Geometry and Tracking and is a project that evolved from the Detector Research and Development Committee (DRDC) at CERN. Different geometries and physics models can be included to test experiments or make proof of principle studies based on Monte Carlo methods [40, 41]. Geant4 allows the implementation of geometrical objects with different properties and various physics models. By a process called *tracking*, the progression of particles in the defined objects can be simulated and all values of interest (e. g. energy, position, reaction type) can be saved.

In the field of proton therapy and especially prompt gamma analysis, the Geant4 toolkit is used to recreate a clinical environment to test different setups of detectors and targets. In this thesis, Geant4 is used to collect data for prompt gamma energy and time spectra to analyse them with different methods.

3.2 Physics Lists

The physics models for nuclear reactions are provided by so-called physics lists. For different applications there are recommended lists that contain appropriate models for this specific use case [42]. Until today, there is no dedicated physics list for proton therapy so that there are different options to choose from. This topic is discussed for example in [16]. Given these considerations and tests, it seems

reasonable to use the list QGSP_BIC_EMY as it provides a feasible description of the experiment and evaluated cross section data from the Cross Section Evaluation Working Group (CSEWG) [43]. The list provides the binary cascade (BIC) model [44] that handles reaction below 10 GeV and also includes the precompound (PRECO) model for low-energy (under 170 MeV) proton-nuclear inelastic interactions. The models for electromagnetic interactions such as Compton scattering or pair production are described in the standard electromagnetic physics list option 3 (EMY). The interactions of nucleons are described with the quark gluon string precompound model (QGSP). It describes high energies from 12 GeV to 100 TeV. A description of the different models can be found in the Geant4 Physics Reference Manual [45].

As it is already tested and commonly used in hadron therapy, this list is used for the simulations in this thesis. Additionally, the discussion in [16] indicates that the important properties – i. e. the existence of discrete energy lines and agreement of the general trend of the spectrum with the experiment – are given so that the results of the simulation are suited for proof-of-principles analysis of the methods presented in Chapter 4.

3.3 Setup of the Simulation Geometry

In this thesis, the version 10.04.p0 of Geant4 is used. As a basic test for determination methods, the setup of the simulation is kept simple. A schematic representation can be seen in Figure 12. The experimental hall only includes the target and the detectors as geometrical objects. All is positioned in a vacuum. To improve the statistics and thereby decreasing the simulation time, a ring of detectors is chosen instead of only one detector. For all the simulation runs, the ring of detectors is facing the centre of the target and is positioned at 90° to the centre. Based on the geometry, this ring consists of 24 detectors which are evenly distributed around the target. That means that the simulation of 10^9 protons in this setup is the same as simulating $2.4 \cdot 10^{10}$ protons with just one detector in terms of gamma detection. This has to be kept in mind for the statistical analysis in Chapter 6. The detectors are *sensitive* so that Geant4 saves time, position, energy and interactions of the particle in the object during the simulation. Cerium(III) bromide (CeBr_3) is selected as material of the detectors since this material is used for the experiment at OncoRay in Dresden in Section 3.4. The size of the detectors is cylindrical 50.8 mm in diameter and 50.8 mm length ($\varnothing 2'' \times 2''$). They are positioned at a distance of 228 mm to the centre of the target. For the simulation any time resolution of the detector is ignored and not implemented. Additionally, Geant4 uses the front plate of the detector as the detection timing of the photons to eliminate the finite expansion of the detectors as an influence on time. Therefore, the simulation and tests represent an ideal case in terms of time resolution of the detector and show the best attainable result. However, it must be noted that there will always be a time width of the proton bunches that prevents reaching the ideal case. This time width is also not simulated. The target,

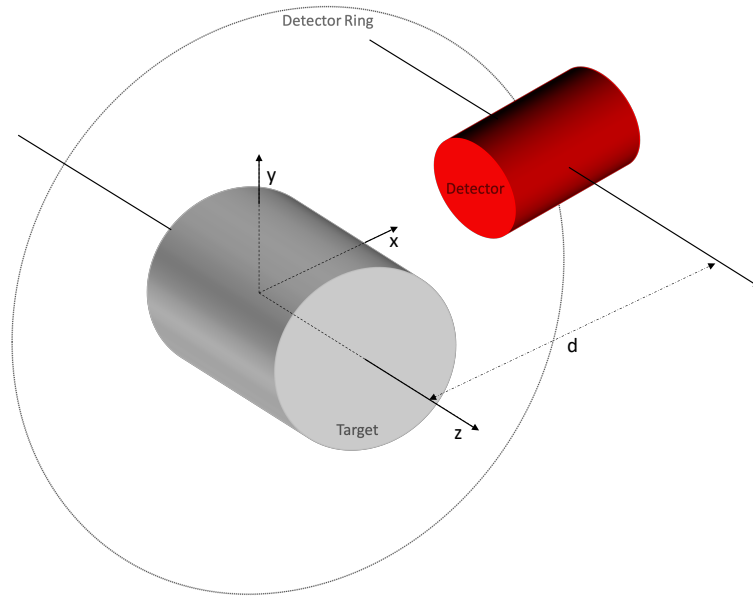


Figure 12: Schematic representation of the simulation setup with the target and one of the detectors in the detector ring in vacuum.

like the detectors, is also *sensitive* and is cylindrical with a fixed diameter of 100 mm so that photons have to cross the same amount of material in all directions. The material and length of the target can be selected freely as well as the material and length of additional slices that can be introduced in the target.

The target is irradiated by protons that are produced by a monoenergetic particle source pointing along the negative z-direction as a pencil beam with no diameter.

Some of the properties of the simulation can be changed by a macro file. The material of the target can be changed and also the energy of the particle source. Furthermore one or two slices can be introduced inside the target. Each can have a different material. The size of the target, the detectors and the slices is set in the Geant4 code.

3.4 Comparison between Simulation and Experiment

Before the data of the simulation is used to test range verification methods, their properties are analysed and compared to experimental data. This comparison is made to justify the usage of the Geant4 simulator for the test of range verification methods. An isochronous cyclotron with a frequency of 106 MHz is used in the experiment. The cyclotron is installed at the OncoRay proton facility Universitäts Protonen Therapie Dresden (UPTD). The type designation is a Proteus C230 built by the company IBA. For the detector a $\varnothing 2'' \times 2''$ CeBr₃ scintillation crystal is chosen. With an energy resolution of $\Delta E/E = 2.21\%$ (FWHM at 4.4 MeV) for detectors with

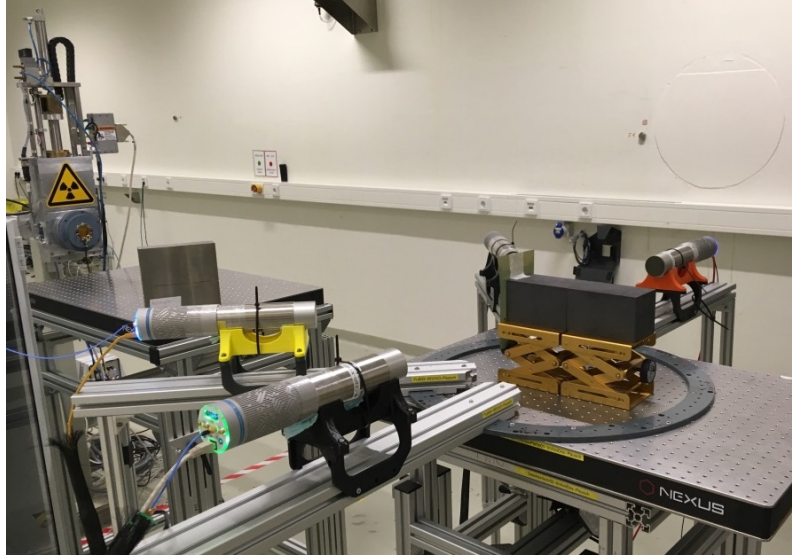


Figure 13: Setup of the experiment with four detector units and a tungsten shield at the Universitäts Protonen Therapie Dresden (UPTD) with a carbon target.

a size of ($\varnothing 1'' \times 1''$) [46] and a short decay time of 18 ns to 20 ns [21] the material is well suited to detect the prompt gammas up to 8 MeV. For the photomultiplier tube (PMT) a Hamamatsu R13089-100 is used. The PMT is plugged on an electronic unit: the Target U100 that was developed for the usage at the UPTD [14]. The U100 is among other things responsible for digitising the signal and the high voltage supply for the PMT.

The beam energy is set to 224 MeV. A PMMA block is used as target. The dimensions are $10 \times 10 \times 30 \text{ cm}^3$. For the experiment four of the above described units are used. They are positioned at 90° , 135° , 225° and 270° to the beam axis with the first two shielded with a tungsten block. The setup can be seen in Figure 13. In order to compare the results of the simulation to the experiment, a time correction and an energy calibration have to be applied to the data. In [31] a detailed explanation can be found of what has been done with these data. Moreover analyses of different material, the angular of the detector and the influence of the collimator are discussed there.

3.4.1 Comparison of the Energy Spectra

For comparing the experiment with the simulation the setup of the experiment is modelled with Geant4. Therefore the setup described in Section 3.3 is changed so that the target, the energy of the source and the distance between detector and target are the same as in the experiment. The environment of the experiment was

not simulated as well as the width of the proton beam and the time resolution of the detector and the proton bunches as it is described in the previous section. The comparison of the energy spectra shows whether all relevant peaks are present in the simulation. In Figure 14 the simulated and the measured energy spectrum up to 12 MeV from a PMMA target that was irradiated with a 224 MeV proton beam are compared. As one can see, the general structure of the experiment spectrum can be found in the simulation. The energy area above 6.5 MeV gets overestimated by the simulation whereas lower energies get slightly underestimated. The area around 3 MeV shows an exception. Here more events are simulated. It can be seen that the peaks of the 4.44 MeV line are as well pronounced in the simulation as in the experiment. In contrast, the lines of 6.129 MeV and 5.2 MeV are underestimated by the simulation and can hardly be distinguished from underground fluctuations.

A similar comparison of targets made of carbon can be seen in Figure 15. Here the simulation also overestimates the energy area above 6.5 MeV but also the area above 5 MeV. The difference of relative frequency is bigger than in the comparison of the PMMA targets. The absence of oxygen in the carbon target should lead to a lower event frequency in this area for the simulated spectrum as it can be seen in the experimental spectrum.

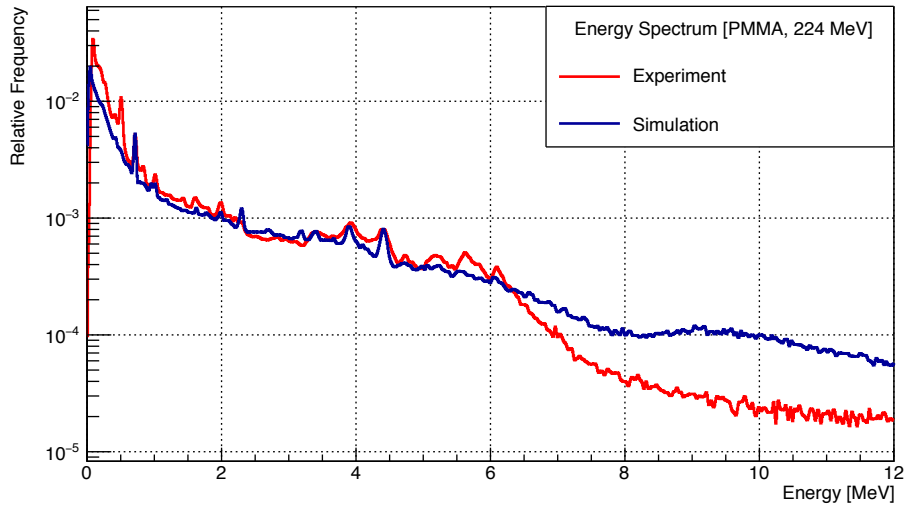


Figure 14: Comparison between the simulated and experimental results of a PMMA target that is irradiated by a proton beam with an energy of 224 MeV. The result of the experiment is scaled to match the 4.44 MeV peak of the simulation and both are normalised to their respective integrals.

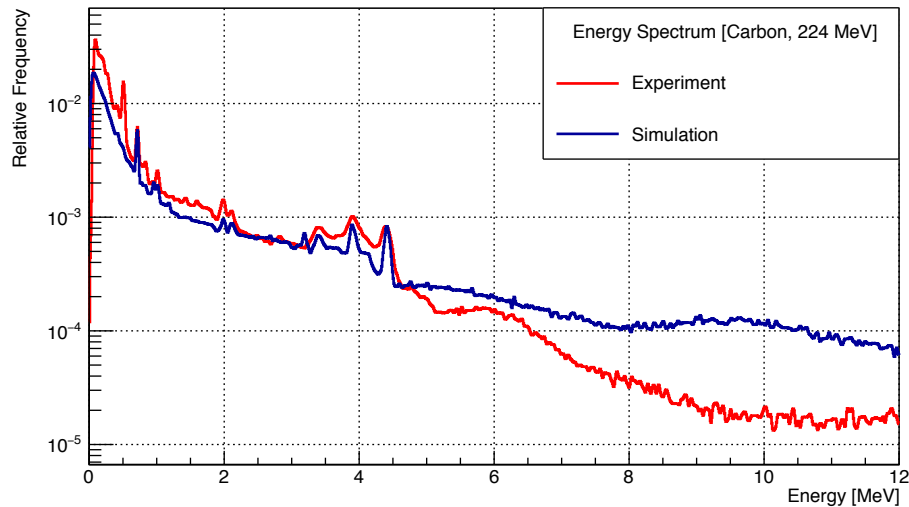


Figure 15: Comparison between the simulated and experimental results of a carbon target that is irradiated by a proton beam with an energy of 224 MeV. The result of the experiment is scaled to match the 4.44 MeV peak of the simulation and both are normalised to their respective integrals.

3.4.2 Comparison of the Energy-Time Spectra

The comparison of the energy-time spectra in Figure 16 shows that the prompt gamma lines are visible as a function of time. The time interval can be correlated to the target as only there prompt gammas are produced. In both cases, the width is roughly 2.5 ns. The simulation is therefore able to reproduce the time structure of the experiment qualitatively.

In Figure 17 the total number of events for each bin on the time axis for different energies and lengths of a simulated PMMA target are shown. It can be seen that the length of the spectrum depends on the size of the target but also on the energy of the protons used. The total number of events increases over time and forms a plateau in targets that are long enough. After that the number of events decreases again. Since the time resolution of the proton bunches and the detector as well as the finite expansion of the detector are neglected, the effect cannot be caused by this. This effect cannot be observed in experiments, since the quantities mentioned above prevent this. With a time resolution of 189 ps at 4.4 MeV [46], the bin width of the simulation cannot be resolved by a CeBr_3 scintillator. In Figure 18 it can be seen that the first bins of such an energy-time spectrum are dominated by gamma energies below 1 MeV. In order to clarify where the effect comes from, further tests and analyses should be carried out. But since it is not relevant for working with real spectra, this is only necessary for tests and calculations with simulated spectra and is considered in this thesis.

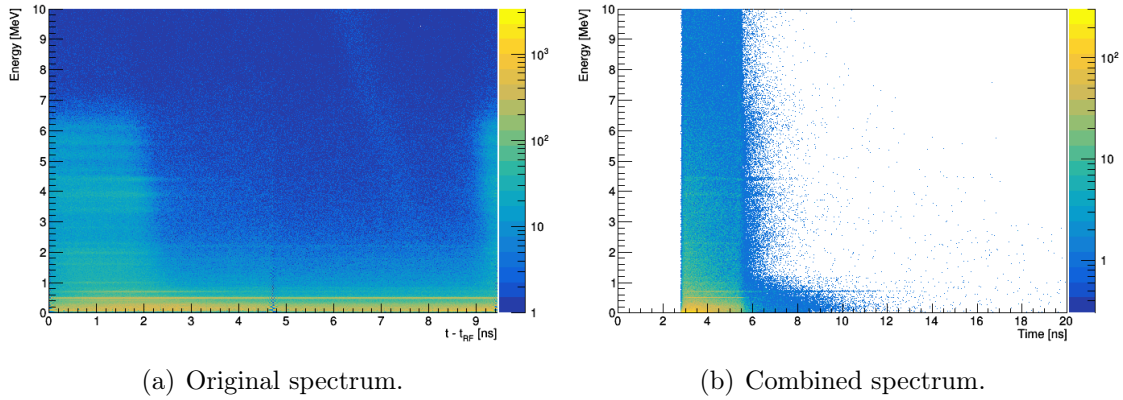


Figure 16: Experimental (a) and simulated (b) energy-time spectrum of a PMMA target that is irradiated with a beam energy of 224 MeV.

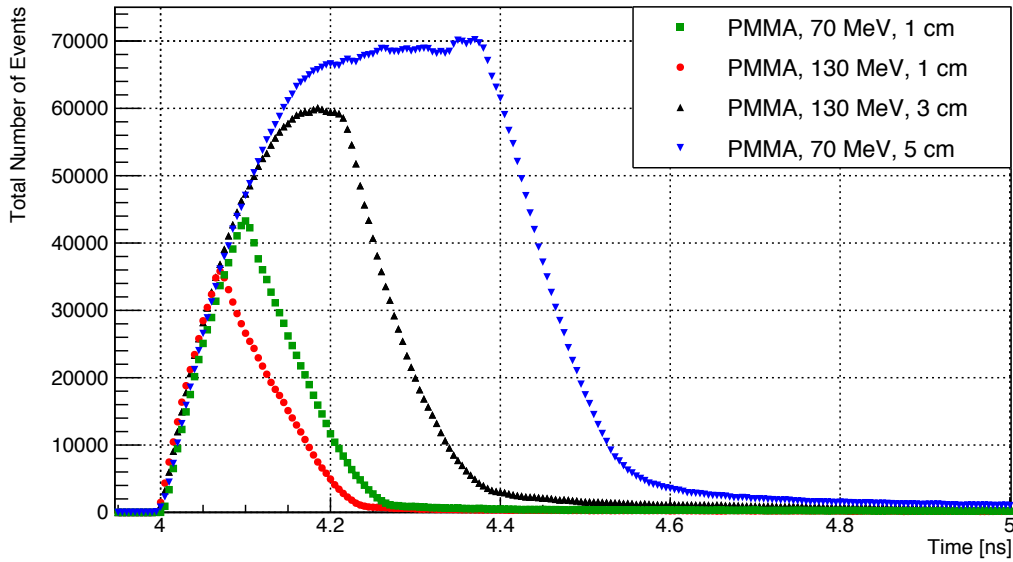


Figure 17: Total number of events for every time of the energy-time spectrum for different simulated PMMA targets.

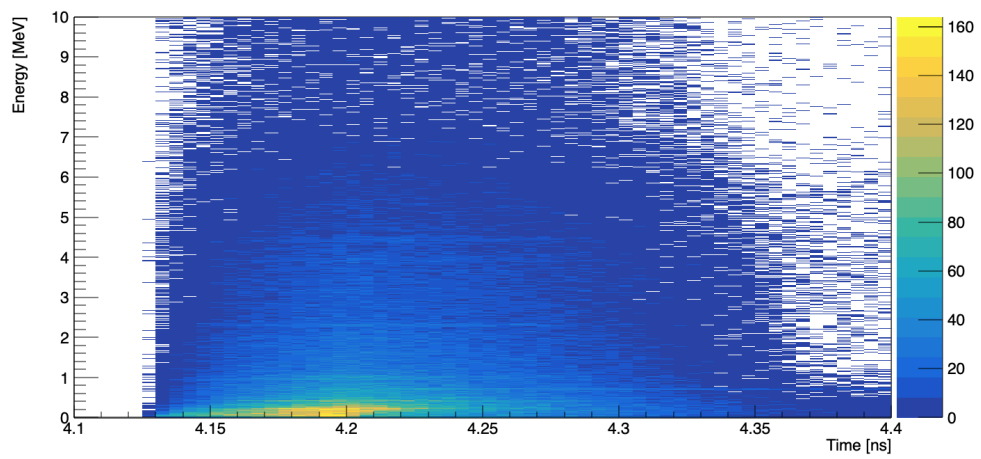


Figure 18: Simulated energy-time spectrum of a 1 cm long PMMA target that is irradiated with a proton beam energy of 130 MeV.

4 Methods to Analyse the Prompt Gamma-Ray Spectra

This chapter gives an overview of the methods used in this work to analyse the simulated spectra. These analyses provide the event number of certain gamma lines which can be used for further calculations in the method described in Chapter 5. For the method in Chapter 6, the analyses described below provide quantifiable values for different targets so that they can be compared against each other. Different approaches are adopted in order to conclude which analysis achieves the best results. The different analyses are presented here only briefly to give an overview of their basic approaches. The analyses are:

- 4.44 MeV peak analysis with background subtraction,
- 3.3 MeV to 4.6 MeV region analysis with background subtraction,
- 5 MeV to 7 MeV region analysis with and without background subtraction and
- chi-square test to determine the similarity of two spectra.

The first two represent the analysis of the prominent 4.44 MeV peak and the respective double and single-escape peak. This line originates from the carbon as well as from the oxygen in the target. Therefore it is well suited to gain information about these two elements. The analysis of the range around the 4.44 MeV peak is included to find out if an analysis of the region instead of the peaks gives better results for spectra with lower event counts. Instead of an analysis of the 6.129 MeV peak also a range analysis is applied for this area. The reason for this is the underestimation of the gamma lines by Geant4 in this energy region (see Section 3.4.1). No background is subtracted for this area because statistical fluctuations could influence the background estimation and by this introduce uncertainties. In addition, as long as the setup of the experiment does not change, it can be tested whether a comparison of different spectra also works without subtracting the background.

4.1 Peak and Energy Region Analysis

In order to determine the number of events of a gamma line, the background of the spectrum must first be subtracted. Then all events of the full-energy, single-escape and double-escape peak are added. For the 4.44 MeV line, an energy interval of 0.15 MeV is selected in which the events are added up. This way of determining the peak areas is, of course, only an estimate, since several lines contribute to the selected interval due to Compton scattering. Additionally, events of the gamma line to be determined are between the peaks in the Compton plateau and are not taken into account. In order to better determine the peak areas, more accurate descriptions

and models of the gamma spectrum must be used. In case of the analysis of an energy region, the background is subtracted and then all events in this region are added.

The background estimation is handled by the TSpectrum class of the data analysis framework ROOT [47]. The class includes a method based on the Sensitive Nonlinear Iterative Peak (SNIP) clipping algorithm [48]. The algorithm takes the values of the spectrum as $v(i)$ with i being the number of bins in the histogram. In the next step the new value for the i^{th} bin is calculated iteratively. For the p^{th} iteration step the value $v_p(i)$ is given by

$$v_p(i) = \min \left\{ v_{p-1}(i), \frac{v_{p-1}(i+p) + v_{p-1}(i-p)}{2} \right\}.$$

Figure 19 gives an illustration of the algorithm for a peak region and outside of a peak region.

Alternatively, $v(i)$ can be calculated by a transformation. For this $y(i)$ represents the count in the i^{th} bin. Then the transformation

$$y(i) \mapsto v(i) = \log \left(\log \left(\sqrt{y(i) + 1} + 1 \right) + 1 \right)$$

is applied. The double log operator is useful for spectra that cover several orders of magnitude and the square root enhances small peaks.

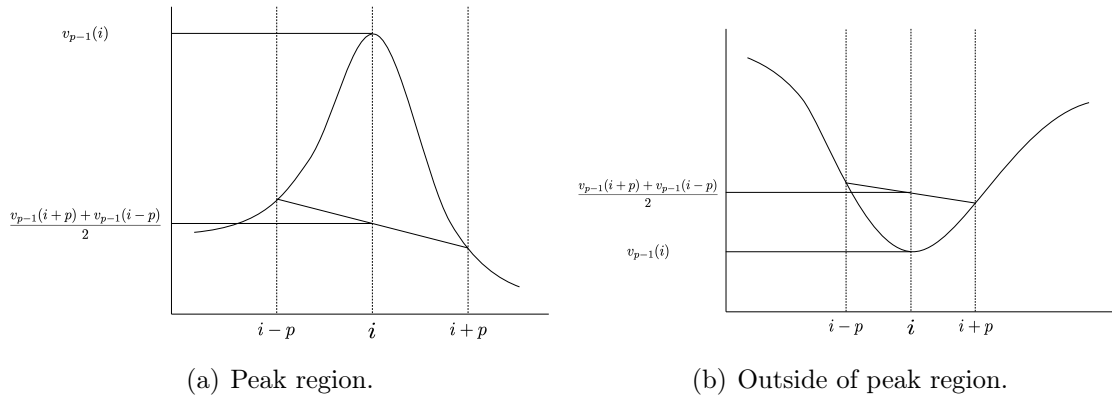


Figure 19: Illustration of the SNIP algorithm for a peak region (a) and outside of a peak region (b). (Adopted from [48])

The method in the TSpectrum class has different options to influence the background estimation (see [49]). For the analysis, all of the options have the default setting. In Figure 20 an example for a background estimation with the TSpectrum class is shown.

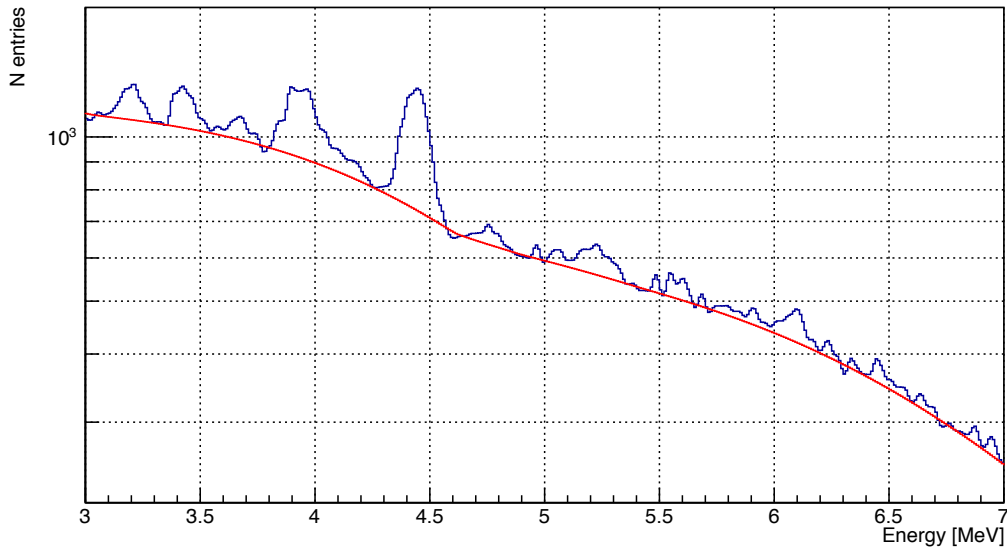


Figure 20: Example of a background estimation with the TSpectrum class for an energy spectrum of a 3 cm long PMMA target that was irradiated with a proton beam energy of 130 MeV.

4.2 Chi-Square Test

For comparing two spectra in terms of their similarity, a chi-square test is used. This is also implemented in ROOT [50]. The closer the result of the test is to 1, the more both spectra follow the same distribution. The test also provides the possibility to compare weighted histograms. As a representation of an experiment the spectra compared in this thesis are not scaled for the chi-square test. So the default setting of comparing two unweighted histograms is applied.

The histograms have the same binning and the same number of bins. The number of bins is given by r and the number of events in each histogram by N and M with

$$N = \sum_{i=1}^r n_i$$

and

$$M = \sum_{i=1}^r m_i$$

where n_i and m_i are the number of events in the i^{th} bin. The homogeneity test has the hypothesis that both histograms of random values have the same distribution. So the probability for a value to be in the same bin i in both histograms is p_i . For

these p_i

$$\sum_{i=1}^r p_i = 1$$

is fulfilled. For the number of events in the i^{th} bin a Poisson probability distribution is assumed. They are given by

$$P(n_i) = \frac{e^{-Np_i} (Np_i)^{n_i}}{n_i!}$$

and

$$P(m_i) = \frac{e^{-Mp_i} (Mp_i)^{m_i}}{m_i!}$$

and therefore the maximum likelihood estimator of p_i is

$$\hat{p}_i = \frac{n_i + m_i}{N + M}. \quad (2)$$

So we get

$$\chi^2 = \sum_{i=1}^r \frac{(n_i - N\hat{p}_i)^2}{N\hat{p}_i} + \sum_{i=1}^r \frac{(m_i - M\hat{p}_i)^2}{M\hat{p}_i} = \frac{1}{MN} \sum_{i=1}^r \frac{(Mn_i - Nm_i)^2}{n_i + m_i} \quad (3)$$

with a χ^2 distribution. The χ^2 value divided by the number of degrees of freedom is used for the evaluation of the comparison.

5 Linearity Method

The first method investigated in this thesis is described in this chapter. The method uses different energy lines of the dominant elements in the human body: carbon and oxygen. For this accurate, cross sections and measurements of prompt gamma-rays are necessary. With this the composition of an unknown target should be directly obtainable during the treatment.

First the effect of the angle between the detector and the target in the simulation is evaluated so that the chosen position of the detector is accounted in the following calculations. Then the method is described. It is based on a linear correlation between oxygen in the target and the number of the 6.129 MeV line. In this chapter it is examined if this correlation is also present in the simulation so that some first calculations can be made in the last section to see if the method is capable to determine the correct composition of a target.

5.1 Angular Distribution of the Simulation

Before the simulations are made, the influence of the detector position is checked so that the central position of the detector to the target (see Section 3.3) is justified. For this a PMMA target with a length of 1 cm is irradiated three times with 10^9 protons and a proton energy of 70 MeV. In the following, the length of the target is given as an indication before the material, so that e. g. a 1 cm PMMA target represents a PMMA target with a length of 1cm and a diameter of 10 ucm. The diameter is the same for all targets. For each of this simulations, the ring of detectors is positioned in the same distance to the target but on another position on the z-axis. The three positions are 90° , 77.63° and 66.32° to the z-axis from the centre of the target. A top view of the setup with the angle between the target and the detectors can be seen in Figure 21.

To see if the simulation with Geant4 assumes an anisotropic effect of the prompt gamma emission the energy spectra are plotted together. First without subtracting the background and then with a background subtraction of the TSpectrum class of ROOT (see Section 4.1). All three spectra in the energy range from 3 MeV to 7 MeV can be seen in Figure 22. As one can see, the background of the simulation with an angle between the detector and the target of 66.32° is lower in comparison to the other spectra in the area above 1 MeV. For lower energies the background for an angle of 90° is the lowest. The comparison after the background is subtracted can be seen in Figure 23. It shows that for the important energy range from 3 MeV to 7 MeV the 4.44 MeV peak is estimated to be of the same height in all three simulations. Only the peaks with energy of 3.2 MeV, 3.416 MeV and 5.65 MeV seem to be lower for the detection under an angle of 66.32° . This confirms statements of an isotropic distribution of prompt gamma-ray reactions at least for the simulation

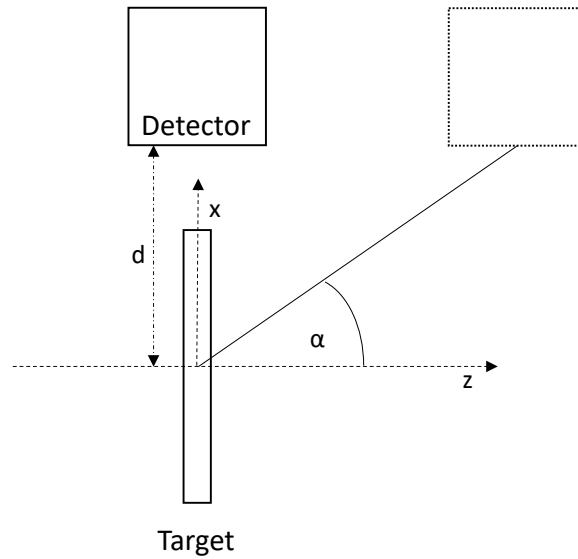


Figure 21: Top view of the detector and target positioning for the simulation to test angular effects. The proton beam is pointing in the negative z -direction. The length of the target is 1 cm and the diameter 10 cm. The distance d between the detector and the target is 22.8 cm. The detector has the dimensions $\varnothing 2'' \times 2''$.

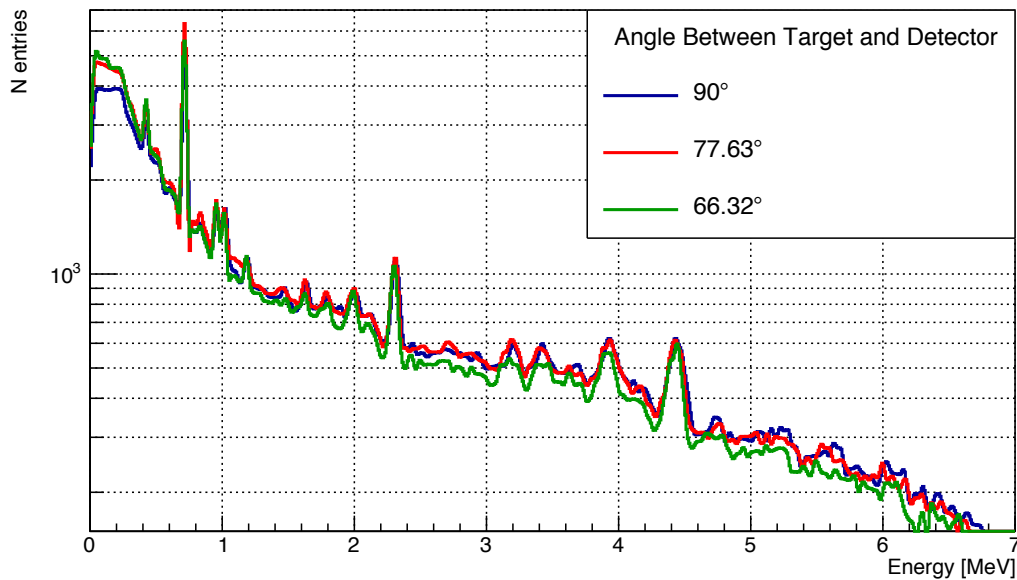


Figure 22: Energy spectra of a 1 cm long PMMA target that is irradiated with a 70 MeV proton beam with three different positions of the detector. The number of simulated protons is 10^9 .

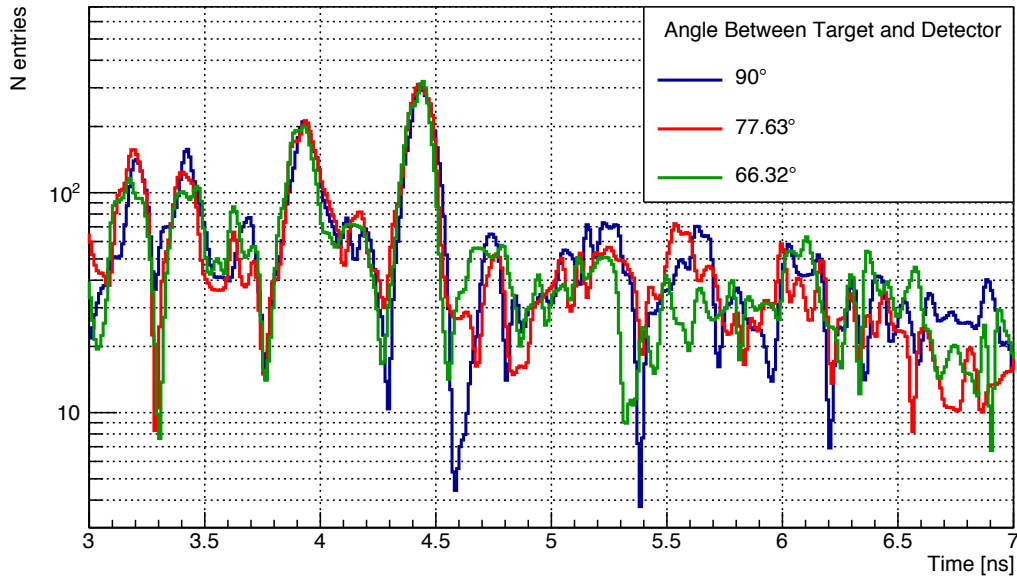


Figure 23: Energy spectra with background subtraction of a 1 cm long PMMA target that is irradiated with a 70 MeV proton beam with three different positions of the detector. The number of simulated protons is 10^9 .

with Geant4 and the physics list QGSP_BIC_EMY. In [31] a similar observation for the experimental setup at the UPTD is made.

Figure 24 shows the total event numbers of the three simulations plotted over time. It can be seen that the arrival time of the gammas in the detector is shifted backwards with decreasing angle, because the gammas have to travel a longer distance. In addition, a broadening of the spectra on the time axis can be observed. The FWHM for a Gaussian fit are 0.127 for 90°, 0.131 for 77.63° and 0.14 for 66.32°. This effect can be explained by the larger difference in the flight time of the photons produced at the beginning and end of the target. In order to minimise the above mentioned effects and thus to make the spectra of targets of different length and material as comparable as possible, the detector in the simulations is aligned centrally to the target. In Chapter 6 in particular, a broadening of the energy-time spectrum could impair the method, since targets of different lengths are used there. For a lower background a position of the detector in backwards direction of the beam is preferable.

5.2 Description of the Method

The linearity method combines the approaches of PGT and PGS (see Section 2.4) to determine the percentage of oxygen and carbon along the path of the protons in an unknown target. As described in Section 2.3.1 the important elements in

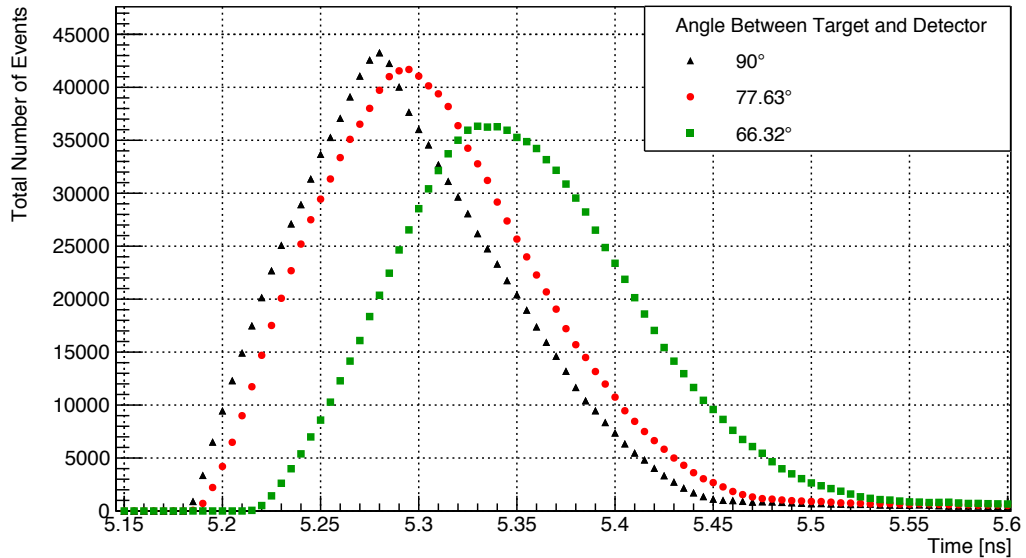


Figure 24: Comparison of the total number of events for every time of the simulated energy-time spectrum of a PMMA target that is measured at three different angles. The proton beam energy is 70 MeV.

proton therapy are oxygen, carbon and hydrogen. The only contribution from hydrogen to the prompt-gamma spectrum is the 2.22 MeV line due to neutron capture [51]. Therefore, to get the composition of the material along the proton path, the percentage of oxygen and carbon needs to be determined. The remainder of the material is then hydrogen and other elements in the human body such as nitrogen or calcium which are neglected in the following tests as they only make a minor contribution to the gamma spectrum due to their small amount in the body.

To determine the elemental composition from a prompt gamma spectrum the linear correlation between the number of detected photons with an energy of 6.129 MeV and the amount of oxygen in the target is used [52]. Figure 25 shows the result of experiment described in [52]. There the total number of prompt gamma-rays emitted per gray rises linear to the amount of oxygen irradiated. The percentage of oxygen in the target was changed, but the dimensions of the target remained the same.

If the percentage of oxygen along the proton path is known, the carbon content can be determined. For this, smaller sections of the proton path have to be analysed instead of the entire path. In order to extract spatial information from the energy-time spectrum, a correlation is established between the location of the reaction and the time at which the gamma arrives at the detector. An accurate calculation of the time it takes the proton to travel the path in the target and the gamma to reach the detector can be performed using the stopping power of the material [39]. First analyses of the simulated spectra without the exact calculation show that for a proton energy of 70 MeV 1 cm in the target can be correlated to about 130 ps in

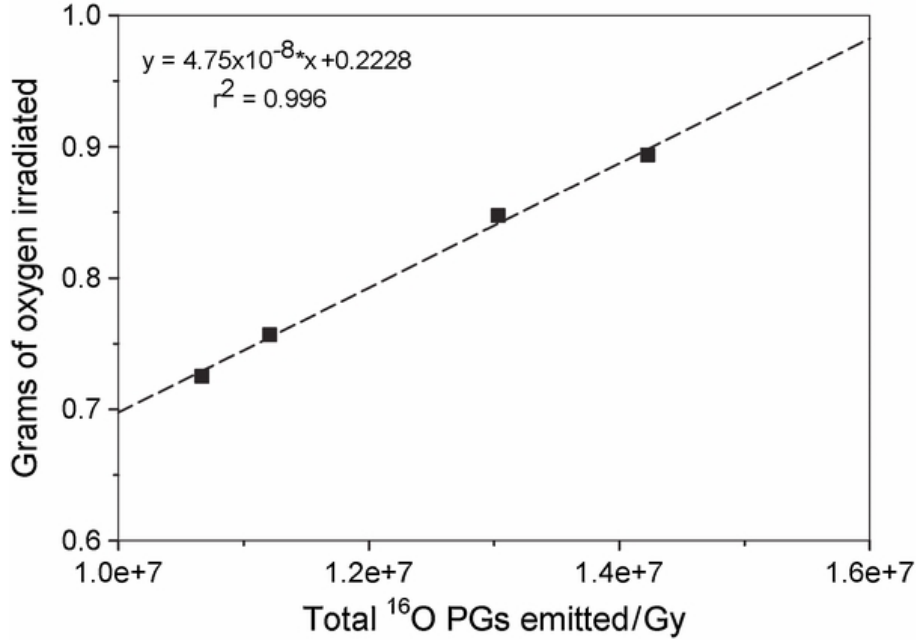


Figure 25: Result of a linear fit of the amount of oxygen irradiated in gram as a function of the total number of measured prompt gammas with an energy of 6.129 MeV. (Taken from [52])

the energy-time spectrum (see Figure 26). For a proton energy of 130 MeV, 1 cm corresponds to approximately 80 ps. In order to be able to make first statements about a possible application of the proposed method in the following, this estimation is sufficient.

In the first step, the percentage of oxygen in the small section of the proton path must be determined as described above. Since the cross section and thus the amount of detected prompt gamma changes with the energy of the protons used, such a linear fit between the amount of oxygen and the resulting amount of prompt gammas must be made for each specific energy interval of the individual path sections. However, since the material and thus the stopping power of these sections is not known, this energy interval must be determined in another way. One possibility is to take the energy interval as given. On the basis of this assumption, the percentage of oxygen in the section f_{O} can then be determined.

With this the number of protons that led to reactions inside the section is then calculated:

$$N_{\text{Proton}} = \frac{N_{6.129 \text{ MeV}}}{\sigma_{\text{O},6.129 \text{ MeV}} \cdot f_{\text{O}} \cdot n_{\text{timeslice}} \cdot d}.$$

$N_{6.129 \text{ MeV}}$ is the number of measured photons in the 6.129 MeV peak, $n_{\text{timeslice}}$ the number of atoms per volume in the timeslice and d the thickness of the slice. $\sigma_{\text{O},6.129 \text{ MeV}}$ represents the cross section between protons and the oxygen nuclei

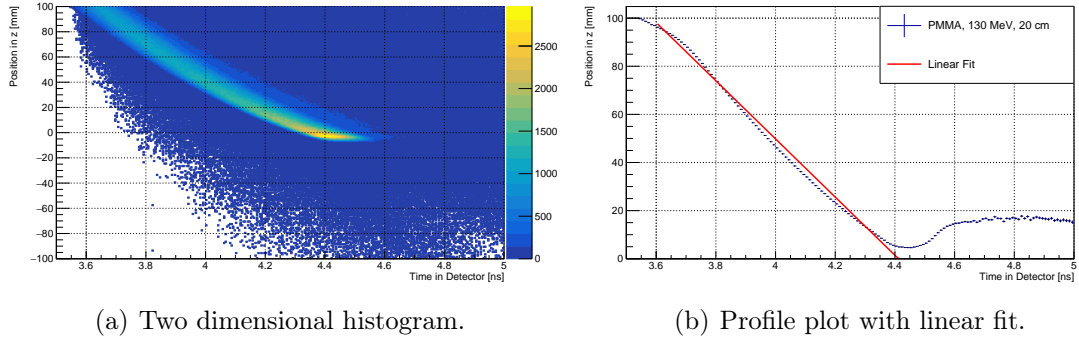


Figure 26: Plot of the position where the photon is created and the time the photon hits the detector as a two dimensional plot (a) and as a profile plot (b) with a linear fit. For the analysis a 20 cm PMMA target that is irradiated with a proton beam with an energy of 130 MeV is used. The results for the linear fit are $p_0 = (533.25 \pm 0.09)$ mm and $p_1 = (-120.87 \pm 0.02)$ mm ns⁻¹.

multiplied by the branching ratio for the 6.129 MeV reaction.

The number of protons can be used to calculate the number of gammas in the 4.44 MeV peak originating from oxygen in the section.

$$N_{O,4.44 \text{ MeV}} = f_O \cdot \sigma_{O,4.44 \text{ MeV}} \cdot n_{\text{timeslice}} \cdot d \cdot N_{\text{Proton}}$$

is used for this purpose. The remaining number of gammas is used to determine the carbon content:

$$f_C = \frac{N_{4.44 \text{ MeV}} - N_{O,4.44 \text{ MeV}}}{\sigma_{C,4.44 \text{ MeV}} \cdot N_{\text{Proton}} \cdot n_{\text{timeslice}} \cdot d}.$$

Here $\sigma_{C,4.44 \text{ MeV}}$ and $\sigma_{O,4.44 \text{ MeV}}$ representing the cross sections for the 4.44 MeV peak of the two elements and $N_{4.44 \text{ MeV}}$ the total number of measured photons with an energy of 4.44 MeV.

By inserting the equations into each other the number of protons in the section, the thickness of the section and the atoms per volume in the section can be eliminated. This leaves a relational equation with the cross sections and the measured number of photons in the two peaks for the fraction of carbon in the section:

$$f_C = f_O \cdot \left(\frac{N_{4.44 \text{ MeV}}}{N_{6.129 \text{ MeV}}} \cdot \frac{\sigma_{O,6.129 \text{ MeV}}}{\sigma_{C,4.44 \text{ MeV}}} - \frac{\sigma_{O,4.44 \text{ MeV}}}{\sigma_{C,4.44 \text{ MeV}}} \right). \quad (4)$$

With the knowledge of the material composition the rest of the spectrum is used to check if the assumed energy range is correct. For this other peaks like the 5.2 MeV or 2 MeV peak can be used. If the number of events in these peaks do not correspond to the amount of gammas created by the determined material composition and assumed

5.3 Linear Correlation between the 6.129 MeV Peak and the Oxygen Amount

energy range, the process needs to be repeated.

Another way to determine the energy range is by using only peaks that originate from the oxygen inside the section of the proton path. The number of photons in these peaks can be calculated with

$$N = f_O \cdot \sigma_O \cdot n_{\text{timeslice}} \cdot N_{\text{Proton}}.$$

Using for example the 5.2 MeV peak and the 6.129 MeV peak one gets:

$$\frac{N_{6.129 \text{ MeV}}}{N_{5.2 \text{ MeV}}} = \frac{\sigma_{O,6.129 \text{ MeV}}}{\sigma_{O,5.2 \text{ MeV}}}.$$

This means that the ratio of the measured events in the two peaks must be equal to the corresponding cross sections. By comparing the cross sections to one another the right energy in the section could be found. If there are multiple points at which the ratios are equal the energy nearest to the previous section is taken.

This way to determine the composition of a section of the whole target is repeated as long as the unknown target is completely reconstructed.

5.3 Linear Correlation between the 6.129 MeV Peak and the Oxygen Amount

To verify the linear correlation between the oxygen content and the 6.129 MeV peak in the simulation targets with different percentages of oxygen but the same dimensions are simulated. All of the simulations use a proton beam energy of 130 MeV and the target has a length of 20 cm and a diameter of 10 cm so that a full absorption of the proton energy happens. In Table 2 the different targets with their respective oxygen amount are shown. Geant4 offers the possibility to create mixtures from different

Table 2: Target composition and respective oxygen amount of the used targets.

Target Composition	Oxygen Amount [%]	Carbon Amount [%]
Carbon	0.0	100.00
PMMA (40 %), Carbon (60 %)	5.2	73.32
PMMA (60 %), Carbon (40 %)	7.8	59.98
PMMA	13.3	33.33
Water	33.3	0.00

materials. They are defined by the fraction of mass of each component. This is used to create the two targets as a mixture of PMMA and carbon to generate targets with

different oxygen amounts. Additionally to the above mentioned targets, a target made of polyoxymethylene (POM) is simulated. It has an oxygen amount of 25 % as well as 25 % carbon and is used to verify the method.

As one can see in Figure 27 the linear correlation is also present in the simulation with Geant4. The chi-square value per degree of freedom for the linear fit is 3.63. Instead of the event counts in the 6.129 MeV peak the events in the energy range from 5 MeV to 7 MeV are used because of the underestimation of the peaks in this area by Geant4 (see Section 3.4.1). The values $p(f_O)$ for the different targets are calculated as the event counts in the energy range from 5 MeV to 7 MeV $N_{5-7\text{MeV}}$ in proportion to the events in the range from 1 MeV to 8 MeV $N_{1-8\text{MeV}}$:

$$p(f_O) = \frac{N_{5-7\text{MeV}}}{N_{1-8\text{MeV}}}.$$

This percentage is determined for 10 data sets that are generated from the individual simulation. Each set represents the irradiation of the target with 10^8 protons. The value that is used for the linear fit is the mean value of these 10 sets. The uncertainty is the standard deviation of the smaller sets from this mean value.

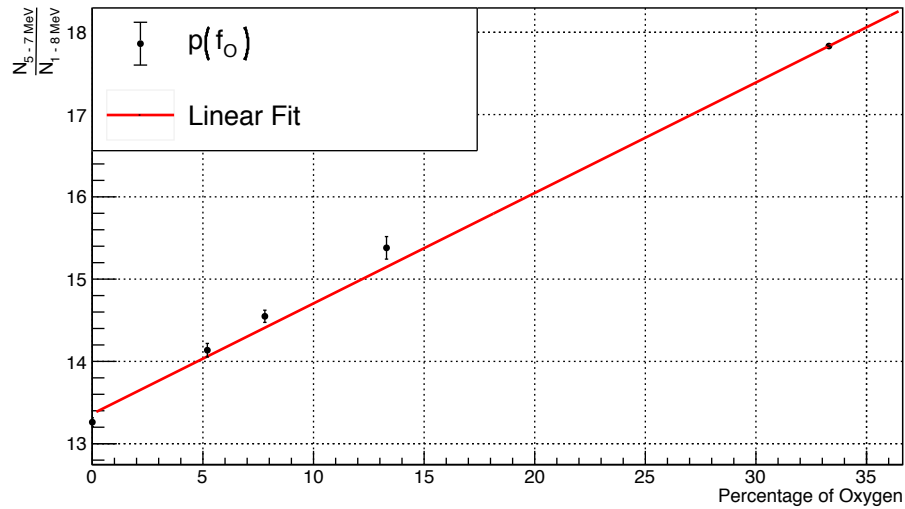


Figure 27: Linear fit of prompt gammas in the energy range from 5 MeV to 7 MeV of targets with different oxygen amount.

For the POM target the percentage of events is $(16.4 \pm 0.1)\%$. This gives a oxygen amount of $(22.1 \pm 0.9)\%$ from the linear fit. As discussed in Section 3.4.1 the amount of events in the area for the carbon simulation is higher in comparison to the experiment. So this point should be lower whereas the other values should be higher as the peaks are underestimated.

Although the accuracy can be improved, this first test shows that the linear correlation is one possible candidate for a starting point to determine the composition

of an unknown target. However, the method must be extended to the smaller structures inside the target which results in lower statistics. Further tests with these structures should be made to see if such a linear correlation can be created with lower event numbers.

The linear fit is also done for the carbon amount in the targets with the analysis of the 4.44 MeV peak and the respective double and single escape peak (see Section 4.1). The result of the fit can be seen in Figure 28.

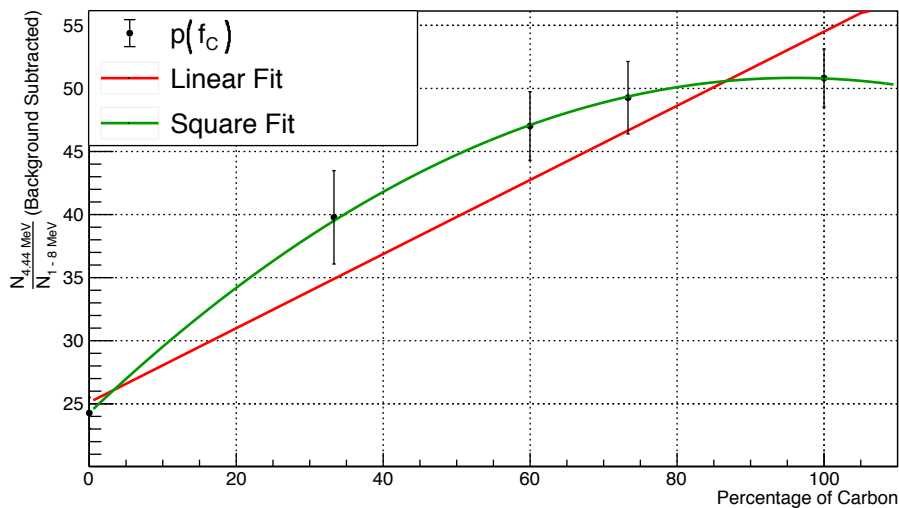


Figure 28: Linear fit of prompt gammas in the 4.44 MeV peak of targets with different carbon amount.

For this the linear fit does not represent the values as well as for the oxygen amount. Using the parameters of the fit the carbon amount in the POM can be determined to $(38.9 \pm 11.2) \%$. For the event counts a square fit is also applied. Even though this fit represents the progression of the values better it is not clear if there is a correlation between the percentage of carbon and events in the 4.44 MeV peak. The reason for that is most probably that the events in this spectral line do not only originate from the carbon in the target but from the oxygen as well. Therefore the plot in Figure 28 should be three dimensional including the percentage of oxygen in the target. One way to determine the carbon amount in an unknown target is by decoupling the oxygen and carbon contribution to the 4.44 MeV region like it is described in the last section.

5.4 Analysis of a Target

To test if the method can be expanded to smaller slices of a target, a 3 cm PMMA target is simulated with a proton beam energy of 130 MeV. Based on the approximation that 80 ps of the energy-time spectrum correspond to roughly 1 cm in the

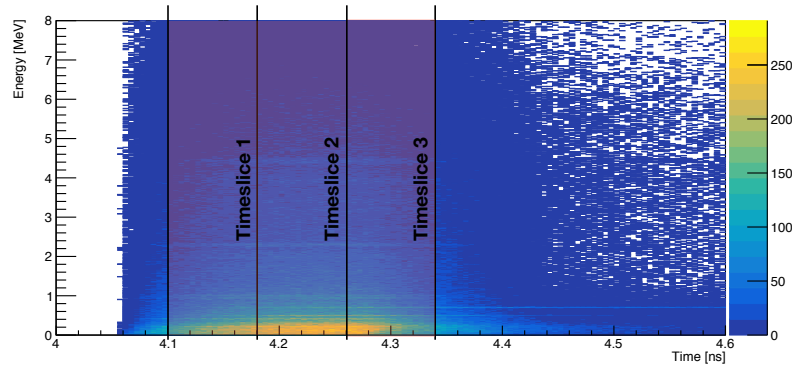


Figure 29: Energy-time spectrum of a 3 cm long PMMA target that is irradiated with a proton beam with an energy of 130 MeV and separated in three smaller parts by 80 ps time frames.

target, the resulting energy-time spectrum of the detected prompt gammas is divided in three parts (see Figure 29) so that each of the timeslices represents 1 cm of the target.

In the following, only an estimation is made if the result of Equation 4 goes in the right direction and could give the correct amount of carbon in the target. As discussed in Section 3.4.2 the energy-time spectra show a energy depended rise-up and fall-down effect at the beginning and the end of the spectrum. Therefore it is not clear where the first slice starts when looking at the prompt gamma spectrum. Additionally, in this test cross sections from [23] are used and not the ones from Geant4 as they were not available for this test. The number of events in the 4.44 MeV peak and the energy area from 5 MeV to 7 MeV are determined like it is described in Section 4.1 with a background estimation from the TSpectrum class of ROOT. The background estimation is included to get an estimation of the peak area in this energy region. But as long as a more accurate description of the background is not made this is also only an approximation. All these inaccuracies lead to an estimation of an uncertainty of 15 % on all the variables in Equation 4. The values for these variables including their uncertainty can be seen in Table 3. Although the events in the area from 5 MeV to 7 MeV are taken the cross section for the 6.129 MeV peak is chosen because of the general underestimation of the peaks in this area (see Section 3.4.1). Because of this bad representation of the oxygen peaks the process to gain the correct energy range for the sections is not done by the linear fit described before. For this first approximation the amount of oxygen is set to be known and has also an uncertainty of 15 %, therefore the value is $(13 \pm 2) \%$.

The results for the three slices are: $(60 \pm 29) \%$, $(58 \pm 27) \%$ and $(43 \pm 20) \%$. PMMA has a carbon content of 33.3 %. For all slices the correct amount of carbon is within the range of uncertainty. Of course there is a lot of room for improvement so that better and more accurate results should be achievable.

Table 3: Values for the number of events and cross sections that are used in the calculation of the carbon amount in the three 1 cm slices in a 3 cm PMMA target.

Variable	Timeslice 1 130 MeV to 123 MeV	Timeslice 2 123 MeV to 115 MeV	Timeslice 3 115 MeV to 108 MeV
$N_{4.44 \text{ MeV}}$	3588 ± 538	5159 ± 774	4322 ± 648
$N_{5 \text{ MeV} - 7 \text{ MeV}}$	1644 ± 247	2238 ± 336	2153 ± 323
$\frac{d\sigma_{\text{O}, 6.129 \text{ MeV}}(90^\circ)}{d\Omega}$	$(2.3 \pm 0.3) \text{ mb sr}^{-1}$	$(2.4 \pm 0.4) \text{ mb sr}^{-1}$	$(2.4 \pm 0.4) \text{ mb sr}^{-1}$
$\frac{d\sigma_{\text{O}, 4.44 \text{ MeV}}(90^\circ)}{d\Omega}$	$(1.1 \pm 0.2) \text{ mb sr}^{-1}$	$(1.2 \pm 0.2) \text{ mb sr}^{-1}$	$(1.2 \pm 0.2) \text{ mb sr}^{-1}$
$\frac{d\sigma_{\text{C}, 4.44 \text{ MeV}}(90^\circ)}{d\Omega}$	$(0.9 \pm 0.1) \text{ mb sr}^{-1}$	$(1.0 \pm 0.1) \text{ mb sr}^{-1}$	$(1.1 \pm 0.2) \text{ mb sr}^{-1}$

5.5 Summary and Discussion

In this chapter, the first method for determining the composition of material irradiated by protons was presented. Previously, the influence of the angle between detector and target on the gamma spectra was analysed. It could be shown that the simulated energy-time spectra with a smaller angle have a broader time distribution. Furthermore, the gammas reach the detector later due to the larger distance to the target. Additionally, it could be shown that the important 4.44 MeV peak and the energy region from 5 MeV to 7 MeV are isotropically simulated by Geant4. In order to minimise effects on the spectra, a centred position of the detector to the target was chosen. The linear dependence of the number of gammas with an energy between 5 MeV to 7 MeV on the percentage of oxygen of a target required for the method could be shown for the simulation. A first test with the material polyoxymethylene confirmed the possibility to determine the oxygen content of a target with the help of the gamma number in the area mentioned above, but left room for improvement of the accuracy. In the last section, a first estimating calculation with large uncertainties was performed for a 3 cm long PMMA target. Although the calculated values were far above the expected carbon value, the actual percentage was within the uncertainty limits. Thus it could be shown that the method presented can theoretically be used for the determination of material compositions. However, further tests have to be carried out. For example, the cross sections used by Geant4 should be determined in order to perform a more precise calculation. In addition, the determination of the peak areas of the individual peaks should be improved in order to calculate with accurate gamma numbers. Afterwards, tests should be performed with a time resolution of the detectors and the time structure of the proton bunches to check whether the method can still be applied. The challenge here will be to assign the local structure in the target to certain sections in the energy-time spectrum.

6 Template Method

This chapter covers the second method examined in this thesis. The idea is to reconstruct an unknown target using so-called templates to determine its composition. Instead of relying on physical principles to calculate the exact composition, this method tries to reproduce the correct composition and to determine whether this type of reconstruction was successful by comparing the spectra. This chapter describes the method of reconstruction and how the templates can be created. To test the method, different targets are simulated. This includes shorter targets of 3 cm that are irradiated with a 130 MeV proton beam as well as targets which contain the full proton path especially the Bragg peak with a beam energy of 70 MeV. In both cases PMMA targets were used and slices of two different material (carbon and water) of 1 cm thickness are inserted in the central part of the larger PMMA target to test the capability of the template method.

First it is checked whether the different comparative analyses for several measurements which were statistically averaged, provide correct results. The longer targets are also used to test how the reconstruction with templates reacts to the Bragg peak and whether the comparative analyses still work. This should give an overview of the different analyses used to compare the spectra and make possible problems of the individual analyses more visible. In the last section, the method is subjected to a statistical benchmark test. This is intended to provide initial estimates of how the method deals with low event numbers, as they will be available in the reality, and whether correct results can then still be achieved. In addition, it is checked whether the method also works consistently with many individual data sets.

6.1 Description of the Method

By irradiating a target that has a certain length and is made of a certain material a specific energy-time spectrum is created. This spectrum depends on the energy of the beam as well as on the material composition of the target (see Chapter 2). A homogeneous PMMA target has a different spectrum than a PMMA target that has a carbon or water slice of a certain length inside the target. In a clinical environment this could be an air cavity, accumulation of liquid, another organ, or bones. The idea now is to reproduce the energy-time spectrum of a large target from the spectra of smaller targets and thus reconstruct the large target. This idea is based on the idea that a large target can be physically composed of smaller target slices. Once the correct proton energy and material have been selected for the energy-time spectra of the slices, the spectrum of the large target should be generated by combining these spectra. In the following, the energy-time spectrum of a known material irradiated with a known proton energy is referred to as a template.

To find the right composition of the unknown target different combinations of

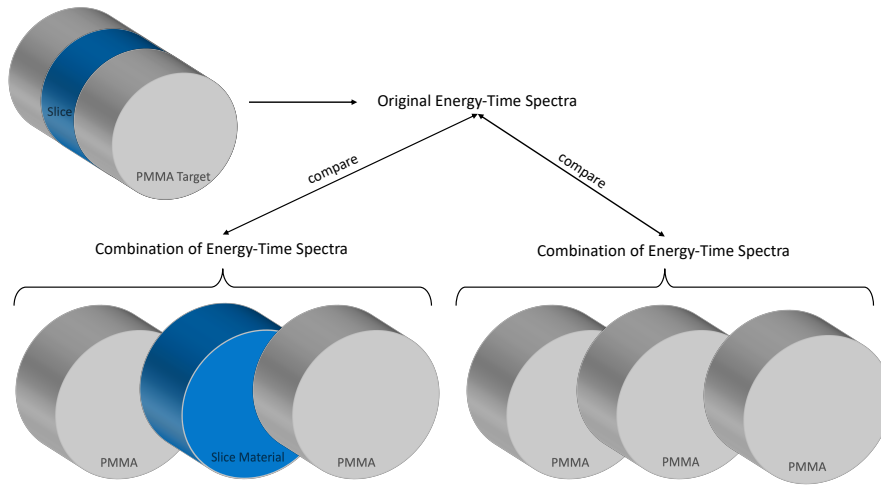


Figure 30: Example for the reconstruction process with different templates. Different combinations of slices are combined and then compared to the original measured spectrum.

smaller targets are created and the energy-time spectra of both are compared. In this way the templates are composed and the result compared until the best combination is found. A simple example of this process can be seen in Figure 30. There the unknown target is a PMMA target with a slice of a different material in the central part. One combination of smaller targets that is compared to the unknown target consists of three PMMA slices. The other one of two PMMA slices and one that represents the material in the unknown target. The latter combination should represent the energy-time spectra of the unknown target better than the combination of PMMA slices.

A starting point for this comparing process would be a CT like it is done in other range verification methods (for example [53]). Then the initial material composition would be known. This should make it easier and faster to search for the correct templates. This is necessary because there is a large variety of materials and proton energies used in proton therapy.

6.2 Construction of the Template Database

To create a database of templates a homogeneous target is irradiated with a proton beam of a specific energy. The resulting energy-time spectrum is then used to create different spectra of the material. They all represent varying energy ranges of the proton beam inside the target and therefore have unique spectra. The templates are created by taking a time interval of a given width and sliding it over the measured energy-time spectrum. This time interval corresponds to a certain energy range of

the protons in the target. By choosing a smaller time interval shorter energy ranges and therefore thinner structures of this material can be represented by the template.

Each of these spectra is influenced by surrounding material due to slower reactions. Therefore it is better to start from simulations or measurements with a thin target that has the width corresponding to the energy range that is needed instead of using a larger target. To get the desired energy range the energy of the proton beam is adapted for each simulation according to the expected mean energy loss in the larger target. For this the Bethe-Bloch formula shown in Equation 1 is used. The calculation is done with the PSTAR program [12, 54]. For example the total stopping power of a proton with 130 MeV in PMMA is $5.86 \text{ MeVcm}^2/\text{g}$. For a density of 1.19 g/cm^3 and 1 cm of target the mean energy loss is 6.97 MeV. Therefore the proton energy for the following slice would be approximately 123 MeV.

6.3 Description of the Applied Test

In the following sections the different analyses are tested. For this, two different simulation are made: targets with a length of 3 cm that are irradiated with a proton beam energy of 130 MeV and 5 cm or 4 cm targets with a proton beam energy of 70 MeV. All targets and the following templates have a fixed diameter of 10 cm. The following targets are simulated:

- 3 cm target and 130 MeV proton beam energy
 - PMMA target
 - PMMA target with a 1 cm carbon slice after the first centimetre of the target
 - PMMA target with a 1 cm water slice after the first centimetre of the target
- 4 cm target and 70 MeV proton beam energy
 - PMMA target with a 1 cm carbon slice after the first centimetre
 - PMMA target with a 1 cm carbon slice after the first centimetre and a 1 cm water slice in the last centimetre
- 5 cm target and 70 MeV proton beam energy
 - PMMA target

They are constructed as shown in Figure 31. Because the CSDA range in PMMA for proton energies of 130 MeV is roughly 11 cm not the full energy of the protons is deposited in the 3 cm targets. The test on these targets therefore shows if the analyses can distinguish between the different materials in the centre of the target. For the 5 cm and 4 cm targets the full energy of the proton is deposited. The CSDA

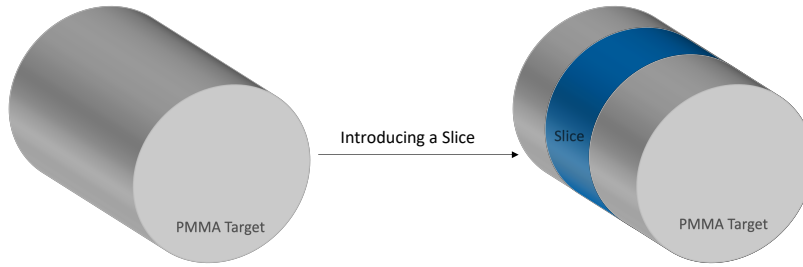


Figure 31: Construction principle of the different targets.

range for protons with 70 MeV in PMMA is 3.5 cm and gets shorter for the targets with the carbon slice. The length of the target was calculated by calculating the energy loss of the protons for each centimetre in the target. For this the Stopping Power determined by PSTAR was used. If the calculated energy is zero or less, the target ends after this slice. It is important to note that the CSDA range and the calculated length do not match. By determining the length like this, it is ensured that the behaviour of the protons is also simulated after the Bragg peak. In addition, the initial energy of the protons of the templates described below is also determined in this way.

For both target types templates in form of 1 cm long slices with the corresponding material and initial proton energy are simulated. The number of simulated protons is always 10^9 . Table 4 shows all templates that are generated.

The energy-time spectra of these templates are combined to represent the spectra of the full target. For this the templates need to be positioned at the right time interval. The beginning of the energy-time spectrum can easily be identified from the two-dimensional histogram. It depends on the geometry of the simulation as well as on the beam energy. The time interval at which the following template must be positioned is determined by the arithmetic mean of the velocity of the protons in the previous section of the proton path. This velocity is used to calculate the time it takes for the proton to pass through this section. The energies are calculated with the Bethe-Bloch formula (see Equation 1). This method is already sufficient to obtain combined spectra in agreement with the fully simulated target.

The so created spectra are then compared to each other so that a conclusion can be made if the target was reconstructed in the right way. For this comparison of the energy-time spectra an arbitrary projection window of 100 ps is created. Note that this window is not related to the correlation between the timing information of the gammas and the corresponding reaction place used in Chapter 5. In this window the two dimensional spectra are projected on to the energy axis. With a stepsize corresponding to the bin width of the energy-time spectrum (here: 0.005 ns) the projection window is moved over the whole spectrum (see Figure 32). Therefore each bin in the following diagrams represents the comparison between 100 ps long

Table 4: Templates for the different targets. The first column shows the target materials in the corresponding 1 cm slices.

Target	Material of Template	Proton Energy of Template
PMMA-PMMA-PMMA	PMMA	130.00 MeV
	PMMA	123.03 MeV
	PMMA	115.77 MeV
PMMA-Carbon-PMMA	PMMA	130.00 MeV
	Carbon	123.03 MeV
	PMMA	111.88 MeV
PMMA-Water-PMMA	PMMA	130.00 MeV
	Water	123.03 MeV
	PMMA	116.76 MeV
PMMA (5 cm)	PMMA	70.00 MeV
	PMMA	58.93 MeV
	PMMA	46.26 MeV
	PMMA	30.93 MeV
	PMMA	9.72 MeV
PMMA-Carbon-PMMA-PMMA	PMMA	70.00 MeV
	Carbon	58.93 MeV
	PMMA	39.46 MeV
	PMMA	22.03 MeV
PMMA-Carbon-PMMA-Water	PMMA	70.00 MeV
	Carbon	58.93 MeV
	PMMA	39.46 MeV
	Water	22.03 MeV

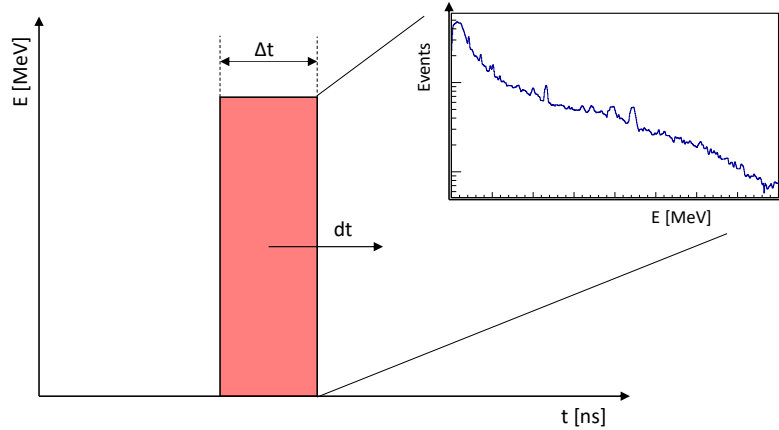


Figure 32: Principle of a sliding window to create energy spectra from an energy-time spectrum. The window has a width of $\Delta t = 0.1$ ns and a stepsize of $dt = 0.005$ ns which represents the selected bin width of the spectra.

windows of the spectra starting at the time of the bin.

For each of these energy spectra a peak analysis of the 4.44 MeV line, an analysis of the region from 5 MeV to 7 MeV, and the chi-square test to compare two histograms implemented in ROOT are applied (see Chapter 4). To get a quantifiable statement which combination of templates represents the original target better a reduced chi-square test is applied on the first two of the above mentioned analyses. For this the results of the combined targets represents the expected data E , the results of the original targets the observed data O and the degree of freedom ν is the number of data points. To calculate the variance, σ^2 , of O the simulation results are divided in ten smaller event sets. Each of these sets represent therefore the simulation with 10^8 protons. The variance is then estimated from these ten data sets. The reduced chi-square is therefore calculated by

$$\chi^2 = \frac{1}{\nu} \sum_i \frac{(O_i - E_i)^2}{\sigma_i^2}. \quad (5)$$

6.4 Test with 3 cm long Targets

The energy-time spectra of the 3 cm PMMA target and the combination of the three corresponding PMMA templates as described before can be seen in Figure 33.

Both histograms are displayed in the time frame of interest, meaning the part of the spectrum where the prompt gammas are detected. In this time range the original spectrum has $1.329 \cdot 10^6$ events and the combined one $1.228 \cdot 10^6$. Although all three templates are simulated with a proton number of 10^9 as well as the 3 cm target, the sum of detected prompt gammas are nearly the same. The reason for

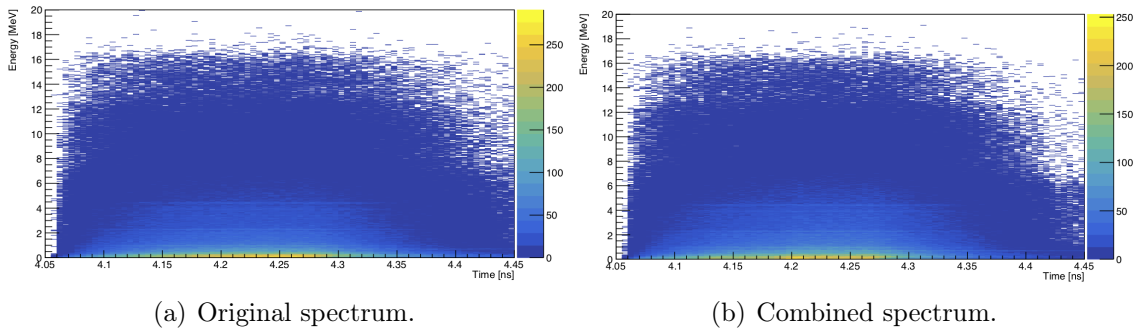


Figure 33: Energy-time spectra of a homogenous PMMA target with a beam energy of 130 MeV. One of the 3 cm long target (a) and one of the combination of three 1 cm long templates (b).

this is that more protons produce a prompt gamma instead of crossing the target without a prompt gamma reaction.

In Figure 34 a comparison of the energy spectra of the three targets can be seen. As expected the event counts for the 4.44 MeV peak are higher for the PMMA target with a carbon slice at the centre. For the other two the peaks are roughly of the same height. For the energy region from 5 MeV to 7 MeV the target with a water slice has the highest event number and the other two targets are closer together. These differences are used to distinguish between the three materials.

Chi-Square Test

For the chi-square test (see Section 4.2) each of the 3 cm targets is compared to the three different combinations of templates. The results for this comparison can be seen in Figures 35, 36 and 37.

For this chi-square between two histograms the integral of the mean chi-square values per bin is calculated. In the following this chi-square test is just called chi-square test and the reduced chi-square (see Equation 5) described in the previous section test is always referred to as reduced chi-square test. The values of the integrals are given in Table 5. For every target the corresponding correct combination of templates shows the best conformity with chi-square values fluctuating around 1 and an integral value of roughly 66 which is the number of bins. The other combinations have stronger deviations from these numbers as their chi-square values in the time frame from 4.1 ns to 4.25 ns rise up to a maximum of 1.6. In all cases the correct combination would be selected as the right one within the range of uncertainty except for the comparison to the PMMA target with a water slice. Here both combinations, the one made from three PMMA slices and the correct combination, shows a similar agreement with the expected material distribution.

The differences in the different comparisons can be explained with the elementally

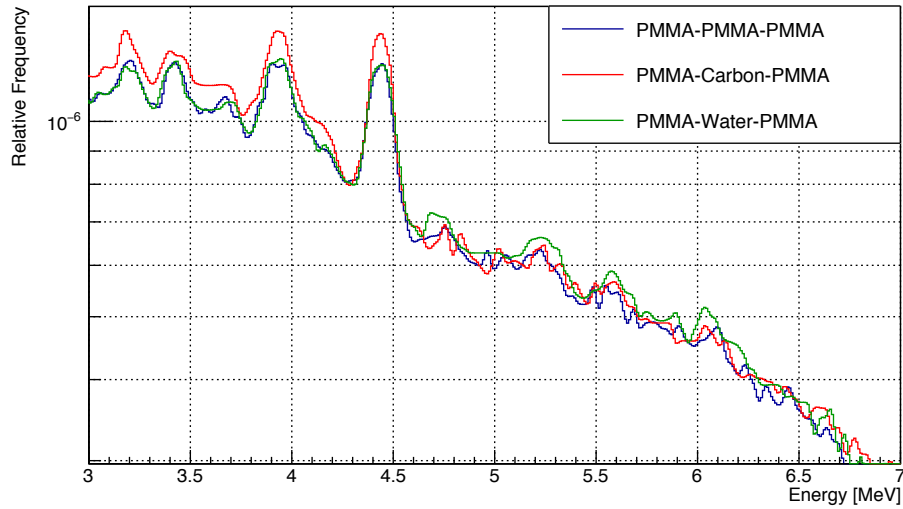


Figure 34: Energy spectra in the energy region from 3 MeV to 7 MeV of the three 3 cm long targets with PMMA, Carbon or Water at the centre of the PMMA target. All targets are irradiated with a proton beam energy of 130 MeV.

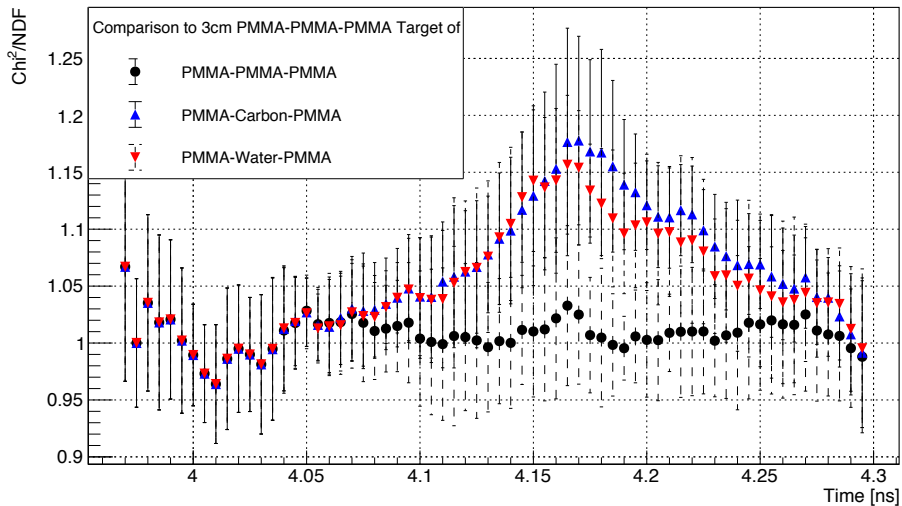


Figure 35: Chi-square test between the 3 cm long PMMA target and the three combinations of templates.

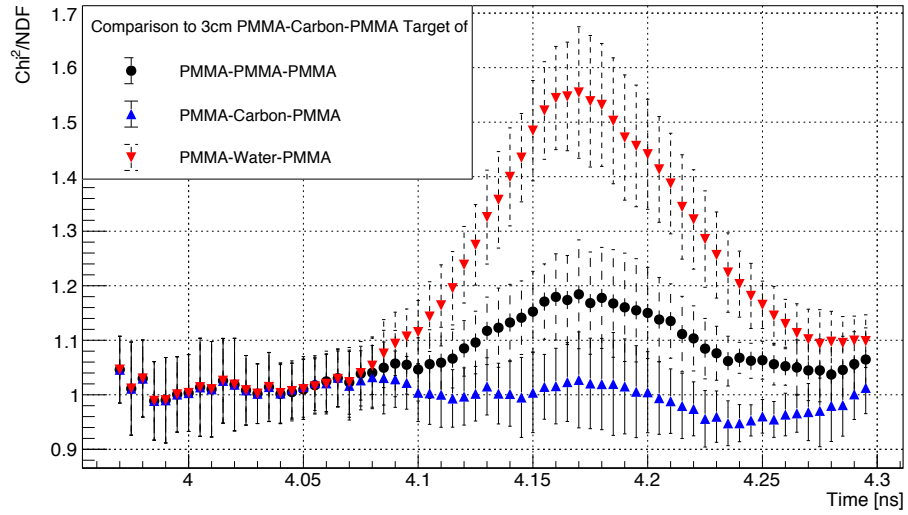


Figure 36: Chi-square test between the 3 cm long PMMA-Carbon-PMMA target and the three combinations of templates.

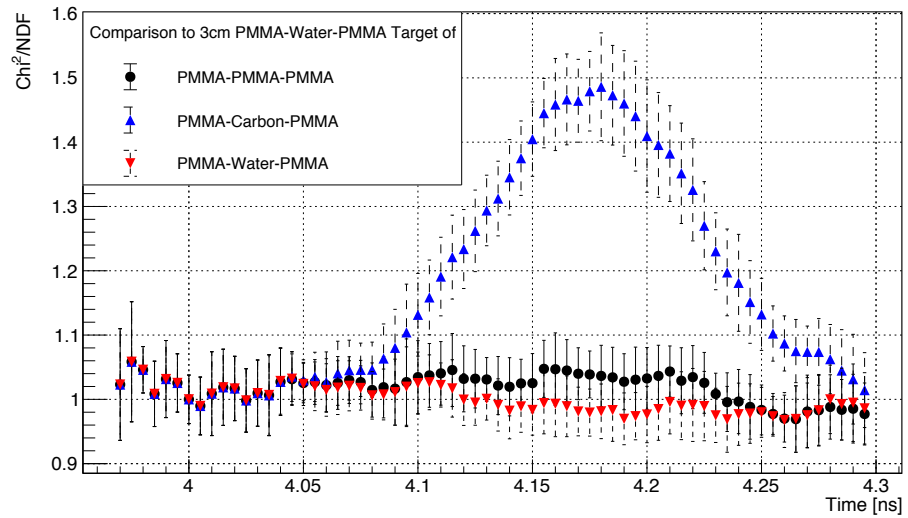


Figure 37: Chi-square test between the 3 cm long PMMA-Water-PMMA target and the three combinations of templates.

Table 5: Result of the chi-square test between the three 3 cm long targets and the different combinations of templates in form of the integral about the resulting chi-square values.

Target	Combination of Templates	Integral
PMMA-PMMA-PMMA	PMMA-PMMA-PMMA	66.5
	PMMA-Carbon-PMMA	69.9
	PMMA-Water-PMMA	69.4
PMMA-Carbon-PMMA	PMMA-PMMA-PMMA	70.6
	PMMA-Carbon-PMMA	66.1
	PMMA-Water-PMMA	78.6
PMMA-Water-PMMA	PMMA-PMMA-PMMA	67.2
	PMMA-Carbon-PMMA	77.5
	PMMA-Water-PMMA	66.0

composition of the slices used. If the composition of these slices differ strongly from one another, like water and carbon, the chi-square test can select between the two. Carbon for example contains no oxygen lines at 5.2 MeV or 6.129 MeV. Slices with a similar composition like PMMA and water, as both energy spectra contain oxygen lines as well as carbon lines, show a greater agreement to one another.

For this statistics and with these three elements the chi-square test can already be used to distinguish between the materials.

4.44 MeV peak analysis

The Figures 38, 39 and 40 show the results of the 4.44 MeV peak analysis with the different 3 cm targets. The number of events in the peak are calculated after the background subtraction like it is described in Section 4.1. This number is then divided by the number of events in the region from 1 MeV to 8 MeV after the background subtraction. The reduced chi-square values between the target and the combinations, that are calculated from the results shown in the above mentioned Figures, are shown in Table 6.

As one can see these values show that the PMMA target and the target with the water slice are represented by their correct combinations. In the case of the 3 cm PMMA target the combination with a water slice shows a similar agreement as the correct combination. For the target with a carbon slice the wrong combination has the lowest reduced chi-square. As Figure 39 shows, starting at 4.1 ns, the events in the 4.44 MeV peak are fewer in the original target in comparison to the

Table 6: Result of the 4.44 MeV peak analysis between the three 3 cm long targets and the different combinations of templates in form of the reduced chi-square value.

Target Composition	Combination of Templates	Reduced Chi-Square Value
PMMA-PMMA-PMMA	PMMA-PMMA-PMMA	1.109
	PMMA-Carbon-PMMA	3.621
	PMMA-Water-PMMA	1.150
PMMA-Carbon-PMMA	PMMA-PMMA-PMMA	2.178
	PMMA-Carbon-PMMA	2.525
	PMMA-Water-PMMA	5.339
PMMA-Water-PMMA	PMMA-PMMA-PMMA	2.791
	PMMA-Carbon-PMMA	15.283
	PMMA-Water-PMMA	1.069

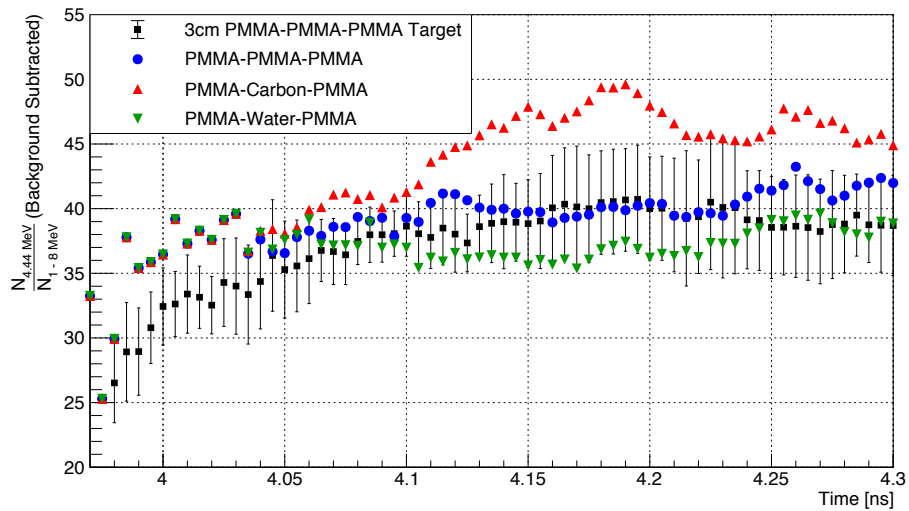


Figure 38: 4.44 MeV peak analysis between the 3 cm PMMA target and the three combinations of templates.

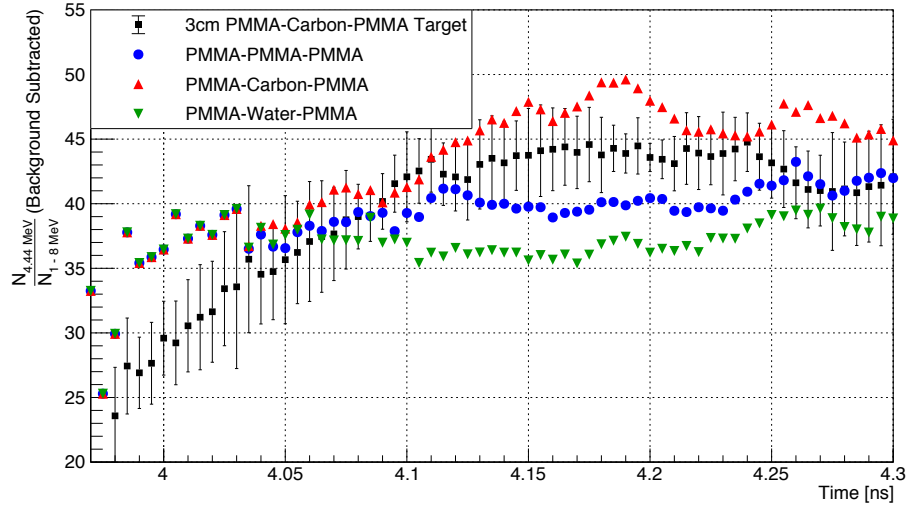


Figure 39: 4.44 MeV peak analysis between the 3 cm PMMA-Carbon-PMMA target and the three combinations of templates.

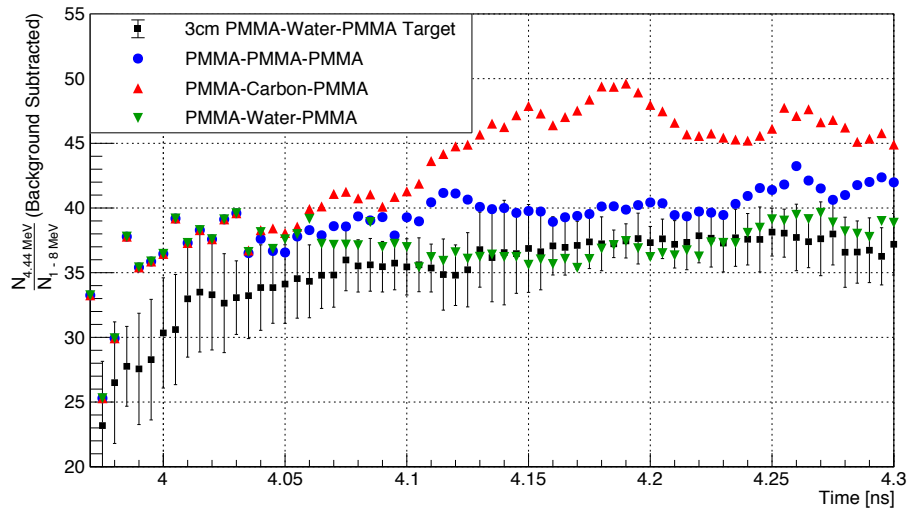


Figure 40: 4.44 MeV peak analysis between the 3 cm PMMA-Water-PMMA target and the three combinations of templates.

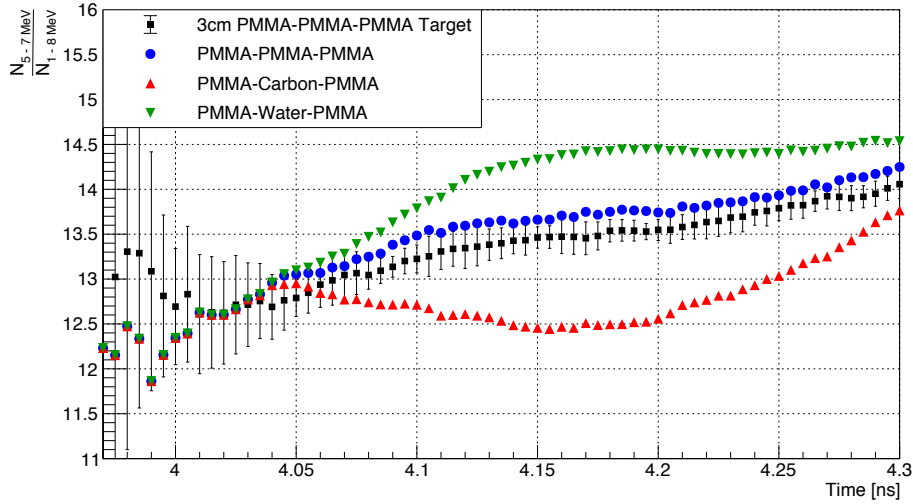


Figure 41: 5 MeV to 7 MeV region analysis between the 3 cm PMMA target and the three combinations of templates.

combination of templates with a carbon slice. This leads to the larger reduced chi-square. Furthermore, the percentage of events in the peak is lower in the time interval from 3.98 ns to 4.05 ns for all three targets in comparison to the template combinations.

One explanation could be the cross sections used by Geant4 and the considered energy range. As the cross section for higher energies of 130 MeV is lower than for lower energies (see Section 2.3) the 4.44 MeV peak is harder to distinguish. This could also explain the higher event rates for the combination with a carbon slice as the higher density could have a larger effect.

Taking the statistical fluctuation into account, the analysis of the peak could lead to the selection of the wrong combination of templates in some cases. Especially in measurements with lower proton numbers the fluctuations could increase and therefore lead to less accurate results with this analysis.

5 MeV to 7 MeV Region Analysis

In the Figures 41, 42 and 43 the analysis of the energy range from 5 MeV to 7 MeV can be seen.

In contrast to the 4.44 MeV peak analysis the three materials can be distinguished even when the fluctuations of the smaller sets are considered. All three follow the expectations as water should have the most events in this range in comparison to the other two materials with carbon having the least amount of prompt gammas. The values in Table 7 confirm this. Only the correct combination of templates has a reduced chi-square near 1.

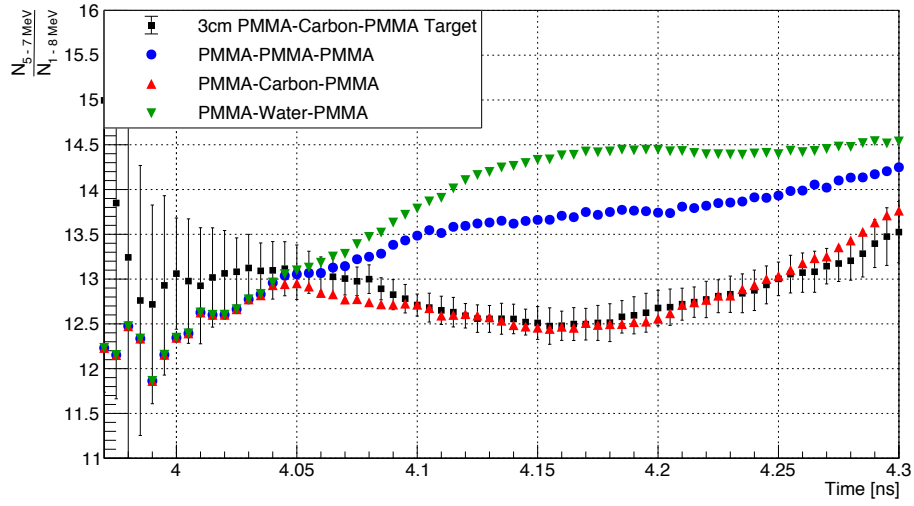


Figure 42: 5 MeV to 7 MeV region analysis between the 3 cm PMMA-Carbon-PMMA target and the three combinations of templates.

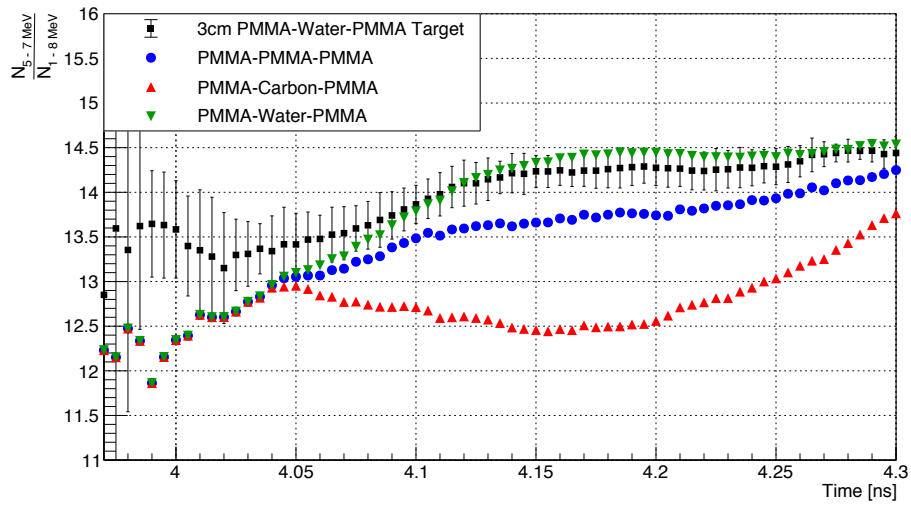


Figure 43: 5 MeV to 7 MeV region analysis between the 3 cm PMMA-Water-PMMA target and the three combinations of templates.

Table 7: Result of the 5 MeV to 7 MeV region analysis between the three 3 cm long targets and the different combinations of templates in form of the reduced chi-square value.

Target Composition	Combination of Templates	Reduced Chi-Square Value
PMMA-PMMA-PMMA	PMMA-PMMA-PMMA	1.499
	PMMA-Carbon-PMMA	19.962
	PMMA-Water-PMMA	17.314
PMMA-Carbon-PMMA	PMMA-PMMA-PMMA	19.803
	PMMA-Carbon-PMMA	0.429
	PMMA-Water-PMMA	46.169
PMMA-Water-PMMA	PMMA-PMMA-PMMA	4.379
	PMMA-Carbon-PMMA	38.609
	PMMA-Water-PMMA	0.884

Summary for the Test with 3 cm long Target

In the given energy range starting with a proton energy of 130 MeV and statistic of 10^9 protons the analysis of the energy region from 5 MeV to 7 MeV can distinguish between all three different materials and the chi-square test and the peak analysis two of the materials. It can also be seen that a combination of different tests and analyses is possible and probably necessary for a broader variety of materials that can be found in the human body. This combination of different analyses is tested in Section 6.6.

Regarding the comparison between the water and the PMMA cavity it needs to be considered that Geant4 underestimates the oxygen lines (see Section 3.4). With a better simulation or in tests with clinical environment the chi-square test could give better results as the peaks can be better distinguished.

In the following section the analysis is repeated with a longer target.

6.5 Influence of the Bragg Peak

The energy-time spectra of the 5 cm long PMMA target and the combination of five 1 cm long PMMA templates can be seen in Figure 44. Again both histograms contain nearly the same number of detected prompt gamma-rays in the shown area: 2 695 801 events in the long target and 2 642 845 in the combined one.

To test the influence of the Bragg peak on the recreation with templates the influence of the last template on the comparison is tested. The chi-square test to

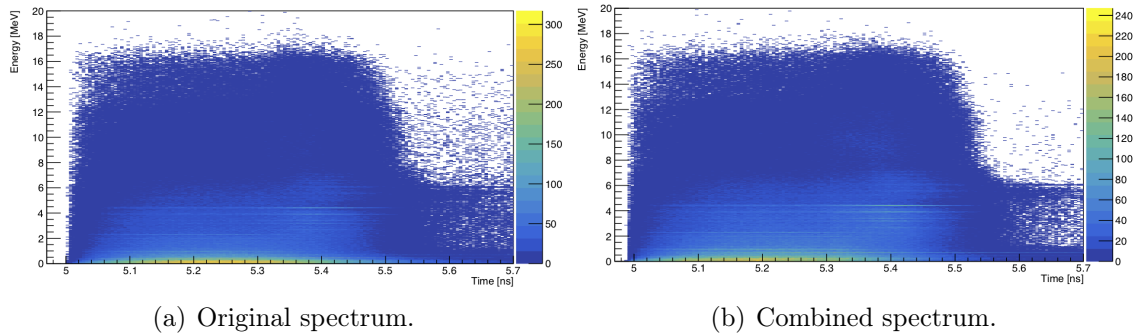


Figure 44: Energy-time spectra of a homogenous PMMA target with a beam energy of 70 MeV. One of the 5 cm target (a) and one of the combination of five 1 cm targets (b).

compare histograms is performed between the following targets and combinations of templates in order to estimate the influence of the Bragg peak:

- 5 cm PMMA target is compared to
 - PMMA-PMMA-PMMA (3 templates)
 - PMMA-PMMA-PMMA-PMMA (4 templates)
- 4 cm PMMA-Carbon-PMMA-PMMA target is compared to
 - PMMA-Carbon-PMMA (3 templates)
 - PMMA-Carbon-PMMA-PMMA (4 templates)
- 4 cm PMMA-Carbon-PMMA-Water target is compared to
 - PMMA-Carbon-PMMA (3 templates)
 - PMMA-Carbon-PMMA-Water (4 templates)

Since the last template for the 5cm PMMA target contains only about 24000 events, its influence on the comparison tests is negligible. Therefore, the 5cm PMMA target is compared once with the first four associated templates and once with the first three templates.

In Figure 45 the results for the comparison with the 5 cm long PMMA target can be seen. The integral of the chi-square values of the two comparisons give 88.9 for the combination of four templates and 123.2 for the combination of three. This indicates that the fourth template is necessary for the correct combination of templates. The reason for this is that the Bragg peak is located in the fourth template, since it is at 3.5cm. The combination with three templates no longer takes this into account.

In contrast, the absence of the last template in the comparisons to the PMMA target with a 1 cm long carbon slice after the first centimetre in the target leads to

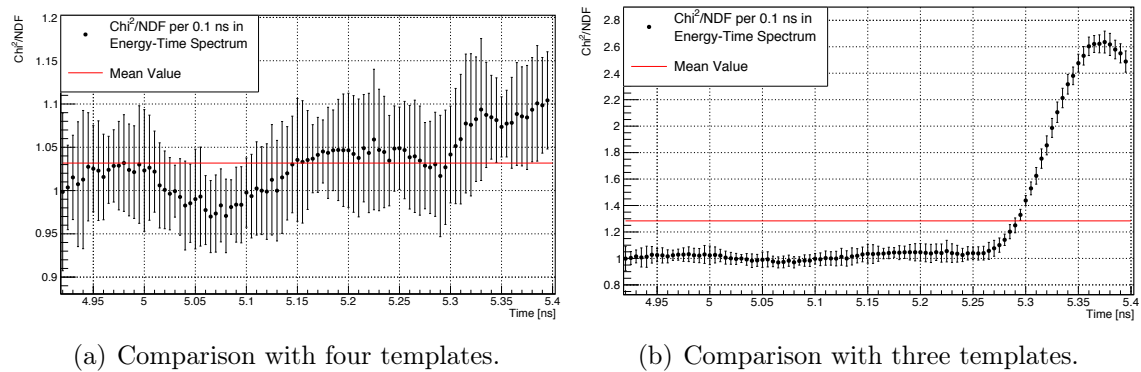


Figure 45: Chi-square test between the 5 cm long PMMA target and the combination of the four associated 1 cm long PMMA templates (a) and three 1 cm long PMMA templates (b).

better results with the chi-square test (see Figure 46). This can again be explained by the Bragg peak. The peak is at a depth of about 3 cm due to the carbon in the target. In the simulation of the whole target, few protons reach this depth and thus few gammas are produced there and this leads to high statistical fluctuations. The comparison with the simulated template therefore leads to bad agreement between the two distributions which is reflected in the high chi-square values. Figure 47 confirms this. The plot shows all proton entries saved by Geant4 in the target. It shows that few protons reach the last centimetre of the target as predicted by the results of the chi-square test. The plot also shows an effect of the simulation at the transition between the two different materials. This effect could be caused by the way Geant4 is simulating the proton path. Normally there is a certain step size after which a new entry for the current particle is set. At the edge this entry could be forced to happen so that there are more proton entries in the histogram in comparison to the rest.

Same results can be found by analysing the last of the three targets. The chi-square test in Figure 48 shows again a better representation of the target when only the first three templates are used.

This considerations lead to an answer regarding the influence of the Bragg peak: because of the low event numbers after the peak a certain answer about the material in this area can not be given by the template method. But for the clinical environment only the material in the path up to the Bragg peak is of relevance to determine the penetration depth of the protons. The tests also show that in order to better resolve and determine the Bragg peak and the region around it, finer structures must be mapped through the templates. Instead of 1 cm, millimetre accuracy would be required.

The comparisons between the targets with a length of 4 cm or 5 cm and the different

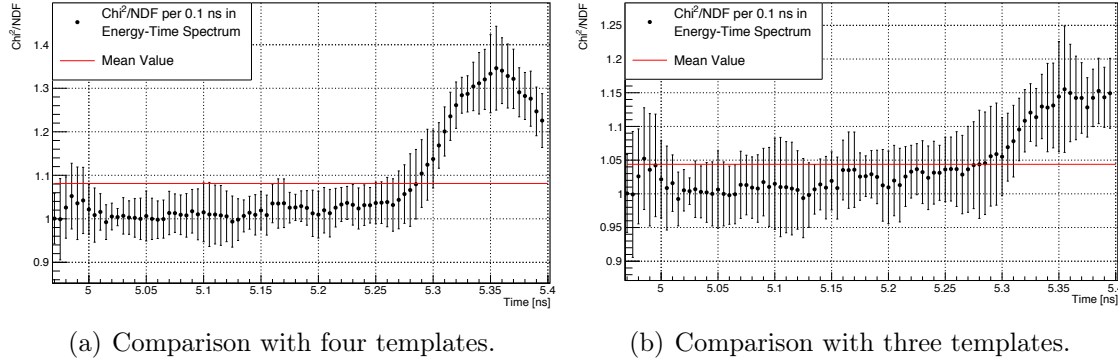


Figure 46: Chi-square test between the 4 cm long PMMA target with a 1 cm long carbon slice after the first centimetre and the associated 1 cm long templates with (a) the last PMMA template and without (b).

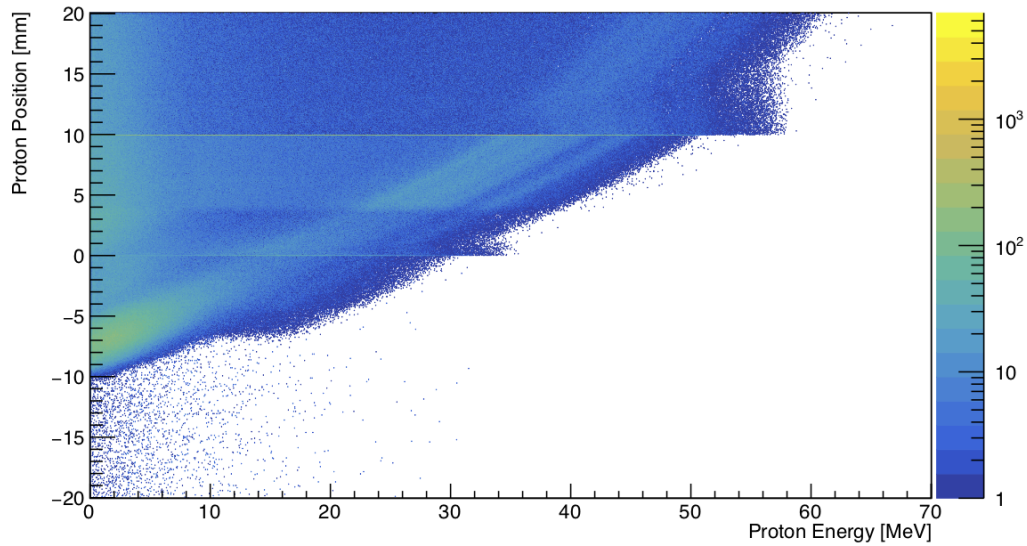


Figure 47: Energy and position of all simulated protons in the PMMA-Carbon-PMMA-PMMA target with a initial beam energy of 70 MeV.

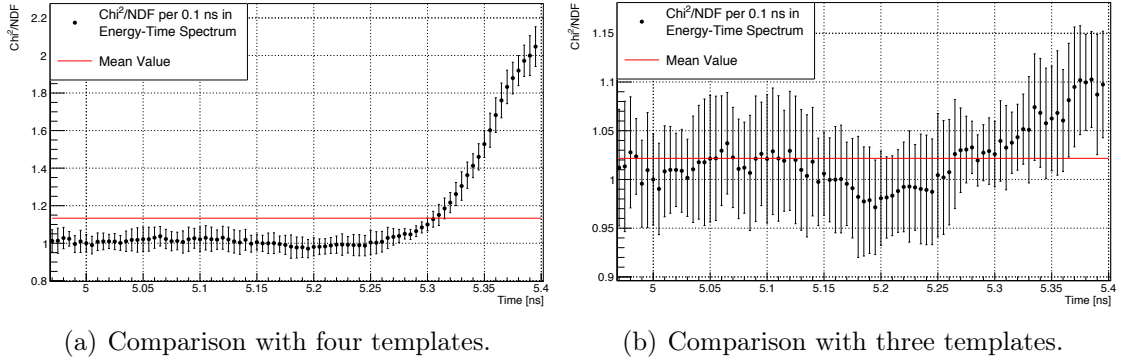


Figure 48: Chi-square test between the 4 cm PMMA target with a carbon slice after the first centimetre and a water slice at the last centimetre of the target with (a) the water slice and without (b) and the associated 1 cm long templates.

combinations of templates only confirm the results of the chi-square tests and the previous section and are therefore not repeated here.

6.6 Statistical Benchmarking

Of course the tests above only show the average of the single analyses. In a real test of the method only one set of events would be tested as a representation of one pencil beam spot. So in the following the different analyses are applied on one small set of events at a time. Again the energy-time spectra is compared in windows of 0.1 ns. For each of these windows the values of the above mentioned analyses is calculated for the original target data and compared to the corresponding value of the different combinations. The relative differences of these two values are then add up for each time window. At the end the combination of templates with the lowest value and therefore with the smallest difference to the target is selected as the best representation. The equation for this process for one analysis is:

$$v(\text{Combination of Templates}) = \sum_k \frac{T_k - C_k}{T_k}$$

with v the value for one possible combination of templates, k the number of bins of the energy-time spectrum, T_k the value of the parameter obtained in the different analyses (e. g. χ^2 , $\frac{N_{5-7\text{MeV}}}{N_{1-8\text{MeV}}}$, ...) using the full target, while C_k is the parameter value using the combined templates.

To test the capability of the different analyses and combinations of them the 3 cm long targets are used. The data obtained from the simulation is again divided in smaller event sets. As mentioned in Section 3.3 the number of protons used

Table 8: Percentage of selection for a certain combination of templates for the three targets with 200 sets with $2.4 \cdot 10^9$ proton for one detector with the chi-square test and the analysis of the 4.44 MeV peak.

Target	Combination of Templates	Chi ² -Test	4.44 MeV-Peak
PMMA-PMMA-PMMA	PMMA-PMMA-PMMA	95.5 %	33.5 %
	PMMA-Carbon-PMMA	4.5 %	0.5 %
	PMMA-Water-PMMA	0.0 %	66.0 %
PMMA-Carbon-PMMA	PMMA-PMMA-PMMA	0.0 %	66.0 %
	PMMA-Carbon-PMMA	100.0 %	27.5 %
	PMMA-Water-PMMA	0.0 %	6.5 %
PMMA-Water-PMMA	PMMA-PMMA-PMMA	50.0 %	10.5 %
	PMMA-Carbon-PMMA	0.0 %	0.0 %
	PMMA-Water-PMMA	50.0 %	89.5 %

for the simulation is 10^9 for 24 detectors corresponding to $2.4 \cdot 10^{10}$ protons for a setup with one detector. The number of protons per pencil beam spot is estimated to be 10^8 [55] that are delivered in roughly 10 ms [14]. Therefore this statistical test is made with the same number of protons. Of course the simulation ignores the detector throughput so that the number of detected prompt gammas of the simulation represent an ideal case. In a realistic environment the statistics used will be lower. To get the amount of prompt gammas corresponding to 10^8 protons, the number of events of the simulation needs to be divided by 240. So the event number of the original target is divided by 10, 240 and 120 for a irradiation of the target with $2.4 \cdot 10^9$, 10^8 and $2 \cdot 10^8$ protons and the detection with one detector. For this, random events from the simulation of the original target are taken to create the sets with the desired number. In total a number of 200 sets for each statistic is created. Additionally to the previous analyses, the analysis of the energy region from 3.3 MeV to 4.6 MeV is included (see Chapter 4).

At first the individual analyses are tested on sets that represent the irradiation of the target with $2.4 \cdot 10^9$ and $2 \cdot 10^8$ protons and one detector. For the sets that represent 10^8 protons only the best analyses are applied.

The Table 8 and 9 show how often one of the combinations was selected for one of the three targets for the $2.4 \cdot 10^9$ proton sets.

As one can see for the event numbers from $2.4 \cdot 10^9$ protons not all tests can distinguish between the three combinations. The best results for the PMMA target and the target with the carbon cavity comes from the chi-square test. For the water

Table 9: Percentage of selection for a certain combination of templates for the three targets with 200 sets with $2.4 \cdot 10^9$ proton for one detector with the analyses of the two energy ranges.

Target	Combination of Templates	3.3 to 4.6 MeV	5 to 7 MeV
PMMA-PMMA-PMMA	PMMA-PMMA-PMMA	55.0 %	97.5 %
	PMMA-Carbon-PMMA	39.5 %	2.5 %
	PMMA-Water-PMMA	5.5 %	0.0 %
PMMA-Carbon-PMMA	PMMA-PMMA-PMMA	6.5 %	0.0 %
	PMMA-Carbon-PMMA	93.5 %	100.0 %
	PMMA-Water-PMMA	0.0 %	0.0 %
PMMA-Water-PMMA	PMMA-PMMA-PMMA	66.0 %	13.0 %
	PMMA-Carbon-PMMA	8.5 %	0.0 %
	PMMA-Water-PMMA	25.5 %	87.0 %

cavity it determines both the PMMA combination and the correct combination in 50 % of the sets. The best test for all three targets is the analysis of the energy range from 5 MeV to 7 MeV as it can determine the right combination in all cases. But for the PMMA target with a water slice in the centre the analysis only selects the right combination in 87 % of the 200 sets. The analyses of the 4.44 MeV peak and the range from 3.3 MeV to 4.6 MeV are less consistent. In two cases they select the right combination of templates for most of the sets and for the other targets not.

With lower event numbers in each set this trend continues. The results for the same test for a irradiation with $2 \cdot 10^8$ protons can be seen in Table 10 and 11.

Most importantly the correct combination of templates are not selected for most of the sets in any of the three cases with the chi-square test. The same is true for the peak-analysis. Here the combination of two PMMA templates and a water template seems to have the least difference against all three targets. In comparison the analyses of the two energy ranges show the best results.

Based on this observations the sets that correspond to 10^8 protons are tested with the two energy region analyses and with a combination of these two to see if by combining different tests a better result can be achieved. The PMMA target is selected correctly in 58.5 % of the 200 sets with the combination of the two analyses. With the analysis of the energy region from 3.3 MeV to 4.6 MeV 57 % of the times. For the target with the carbon slice the combined analysis selects the correct combination in 47 % of the sets and in 80 % for the analysis of the energy region from 5 MeV to 7 MeV. At last for the target with a water slice in the centre of the target the correct combination of templates gets selected 42.5 % for the combined

Table 10: Percentage of selection for a certain combination of templates for the three targets with 200 sets with $2 \cdot 10^8$ protons for one detector with the chi-square test and the analysis of the 4.44 MeV peak.

Target	Combination of Templates	Chi ² -Test	4.44 MeV-Peak
PMMA-PMMA-PMMA	PMMA-PMMA-PMMA	0.5 %	0.5 %
	PMMA-Carbon-PMMA	84.5 %	0.0 %
	PMMA-Water-PMMA	15.0 %	99.5 %
PMMA-Carbon-PMMA	PMMA-PMMA-PMMA	3.0 %	4.0 %
	PMMA-Carbon-PMMA	9.5 %	0.0 %
	PMMA-Water-PMMA	87.5 %	96.0 %
PMMA-Water-PMMA	PMMA-PMMA-PMMA	0.0 %	0.0 %
	PMMA-Carbon-PMMA	100.0 %	0.0 %
	PMMA-Water-PMMA	0.0 %	100.0 %

Table 11: Percentage of selection for a certain combination of templates for the three targets with 200 sets with $2 \cdot 10^8$ protons for one detector with the analyses of the two energy ranges.

Target	Combination of Templates	3.3 to 4.6 MeV	5 to 7 MeV
PMMA-PMMA-PMMA	PMMA-PMMA-PMMA	59.0 %	53.5 %
	PMMA-Carbon-PMMA	22.0 %	26.5 %
	PMMA-Water-PMMA	19.0 %	20.0 %
PMMA-Carbon-PMMA	PMMA-PMMA-PMMA	49.5 %	17.0 %
	PMMA-Carbon-PMMA	44.5 %	82.5 %
	PMMA-Water-PMMA	6.0 %	0.5 %
PMMA-Water-PMMA	PMMA-PMMA-PMMA	52.5 %	28.5 %
	PMMA-Carbon-PMMA	17.5 %	4.5 %
	PMMA-Water-PMMA	30.0 %	67.0 %

analysis and 61 % with the analysis of the energy region from 5 MeV to 7 MeV.

The 100 % selection rate with the peak-analysis for the target with a water slice seen in Table 10 appears in all analyses with lower statistic. So this result is not included as it seems not affected by the targets composition.

6.7 Summary and Discussion

For photon numbers corresponding to $2.4 \cdot 10^9$ protons and one detector and taking the average of the determined results the different ways to compare spectra are suited to distinguish between different materials. This shows that the recreation of a target with templates lead to energy-time spectra that are distinguishable by their progress over time and distribution of the energy lines. Although the analysis in this thesis used 1 cm templates by using thinner templates smaller structures inside the target could be resolved. Because it only depends on the energy-time spectrum itself and not the exact number of events or cross section the method is not depended on measurements and estimations of these variables.

Section 6.5 shows that the Bragg peak complicates the determination of the material in this area of the target depending on the length of the templates. The reason for this is the low number of prompt gammas after most of the protons have stopped.

The statistical benchmarking in Section 6.6 shows that for prompt gamma counts corresponding to real measurements the different methods select the correct combination of templates between 40 % and 80 % of the time. The combination of the two energy region analyses proved to be beneficial in this test. This shows that a combination of different tests and analyses is possible and probably necessary for a broader variety of materials that can be found in the human body. Especially for materials with similar properties analyses of different regions for more information are necessary. The methods that used energy regions proved to be more consistent with lower statistics because they are not depending on peak structures that become more imprecise with decreasing photon counts.

From the two region analyses the analysis without background subtraction is more accurate. In the simulation many sources for the background are not included. So the influence of the background on the accuracy needs to be tested in a more realistic environment.

7 Conclusion and Outlook

In this thesis, two different methods to analyse the material composition of a target are introduced and tested. For these tests, the simulation toolkit Geant4 was used to produce simulations that generate data on which the methods could be tested. A simulation framework was created for this purpose with which time-resolved energy spectra of prompt gamma could be recorded. These so-called energy-time spectra represent the correlation between the frequency of energies deposited in the detector and the arrival time of the gammas in the detector. Since this work is intended to show possible ways to determine the material composition and to estimate whether a further investigation of these methods makes sense, the implementation of the time resolution of the detectors and the time structure of the proton bunches was dispensed with. This results in unrealistic data sets, but it was possible to make first statements about the possibilities of the presented methods. In order to verify that the results of the simulation can function as a substitute for real measured values, i. e. the relative frequencies of the gamma energies and the time structure resulting from the irradiation of the target are simulated, a comparison with the experiment is carried out. The experimental data were recorded at the UPTD at OncoRay. The comparison shows that the general trend of the energy and energy-time spectra can be reproduced by Geant4 v10.04.p0. Nevertheless, some parts of the energy spectrum are not in agreement with the experiment. Most importantly the gamma lines that originate from reactions with oxygen nuclei, namely the 5.2 MeV and 6.129 MeV peak, are underestimated by the simulation. Especially in targets with a low percentage of oxygen, these peaks can hardly be distinguished from the background in the energy spectra. Therefore, not the single line at 6.129 MeV, but the full energy range from 5 MeV to 7 MeV is used to compare two spectra.

The linearity method uses the linear correlation between the irradiated oxygen amount along the proton path in the target and the number of produced prompt gammas with an energy of 6.129 MeV. It could be shown that this correlation is also present in the simulation. With the knowledge of the oxygen amount, it should be possible to decouple the oxygen and carbon content which is responsible for the prompt gammas in the 4.44 MeV peak. One method to do this is motivated in this thesis and relies on the usage of cross sections of the different prompt gamma reactions. By applying this method to smaller parts of the target, the elemental composition of this section of the proton path could be reproduced. The spatial information of the target can be obtained from the energy-time spectrum by correlation of the photon arrival in the detector to the location of the initial reaction. This correlation is energy-dependent, since the time the proton takes to cross the target depends on its velocity. A first test of the linearity method showed that the determination of the material composition is achievable by this way but needs a lot of improvements. To test the linearity method further a better understanding of the cross sections and

processes that are used in Geant4 is necessary.

The template method reconstructs the material composition by comparing the measured energy-time spectrum to different combination of templates. These templates represent parts of a larger target in form of spectra from 1 cm long targets. By putting together these spectra, the original energy-time spectrum is reproduced. The method compares different combinations with the longer targets. Different ways to compare spectra were tested in this thesis. It could be shown that an analysis of an energy region without background subtraction worked most consistently even with low event numbers. The comparison with a chi-square test implemented in ROOT works for spectra with statistics corresponding to an irradiation of the target with $2.4 \cdot 10^{10}$ protons and one detector used. For lower statistics that correspond to statistics of one pencil beam spot (10^8 protons) the chi-square test is less precise. The same holds true for the applied peak analysis. This shows that analysis with only one detector is not sufficient to provide the correct results. However, the evaluated statistics can be improved by using multiple detectors. It could also be shown that the Bragg peak, depending on the size of the templates used, complicates the correct replication of the target. In the test performed with 1 cm long templates, the Bragg peak was within this centimetre which led to worse results of the comparison methods. The test of this method showed that the determination of the correct combination of templates is possible, but it currently lacks a high accuracy and consistency. Also the test was done for three different materials with distinct properties and only for structures that are 1 cm long. The variety of materials inside the human body is much larger and the required precision lies in the range of millimetres. The number of different templates therefore is huge as the database has to cover all different materials for different initial proton energies. One option to improve the algorithm would be to use information from a CT like in [53] to have a starting point for the re-creation process. Additionally, more ways to compare the spectra should be tested. For this a more detailed analysis of the spectra of low gamma statistics should be made to get a better understanding of the behaviour of different materials and elements in general.

Although both methods reviewed already represent promising approaches to determine the material composition of a target, there still is great potential to unlock. Before tests with a real test beam can be performed, further tests with simulations can and should be made. For this the simulation should be improved so that the resulting spectra represent the real physical behaviour. This could lead to a better conclusion for the linearity method which highly depends on exact results for the cross sections. Suggestions to improve the physics list QGSP_BIC_EMY have already been made in [56]. They suggest to use the precompound model with an alternative initial nuclear exciton state of 2 instead of the binary cascade model (see Chapter 3.2). Also instead of the cross sections provided by WELLISH and AXEN [57] for ^{12}C and ^{14}N , the cross section of TRIPATHI *et al* [58] is recommended. Beside just relying purely on Monte Carlo simulations a combination of simulation and

measurements could be used. As is described in [53], the energy distribution of the protons inside the target can be obtained by the simulation and the spectra by using measured cross sections. By this a more consistent statistical result could be achieved as the data would no longer rely on detector geometry and could be adjusted in more ways. In addition, tests must be carried out which take into account the timing resolution and time structure of the proton bunches. Only if a determination of the material composition is successful, if these factors are included, can the found approaches be further pursued.

Of course there is room for other methods to determine the elemental compositions of unknown targets. For example an adjustment from the method used in [53] to the smaller parts of the proton path that are used in the linearity method could be made. By calculating the expected number of events in this part of the target based on a CT, one could calculate the differences and thereby the measured properties of the unknown target or patient by using a least-square-residual minimisation.

8 References

- [1] B. W. Stewart and C. P. Wild, eds., *World cancer report 2014* (International Agency for Research on Cancer, 2014), <http://publications.iarc.fr/Non-Series-Publications/World-Cancer-Reports/World-Cancer-Report-2014>.
- [2] World Health Organization, *Latest global cancer data: cancer burden rises to 18.1 million new cases and 9.6 million cancer deaths in 2018*, 2018, <https://www.who.int/cancer/PRGlobocanFinal.pdf?ua=1> (visited on 02/07/2019).
- [3] R. R. Wilson, “Radiological use of fast protons”, *Radiology* **47**, PMID: 20274616, 487 (1946), <https://doi.org/10.1148/47.5.487>.
- [4] Particle Therapy Co-Operative Group, *Particle therapy facilities in clinical operation*, <https://www.ptcog.ch/index.php/facilities-in-operation> (visited on 02/07/2019).
- [5] Particle Therapy Co-Operative Group, *Particle therapy facilities under construction*, <https://www.ptcog.ch/index.php/facilities-under-construction> (visited on 02/07/2019).
- [6] X. Tian, K. Liu, Y. Hou, J. Cheng, and J. Zhang, “The evolution of proton beam therapy: Current and future status”, *Molecular and clinical oncology* **8**, 15 (2018), <https://www.ncbi.nlm.nih.gov/pubmed/29399346>.
- [7] H. Bethe, “Bremsformel für Elektronen relativistischer Geschwindigkeit”, *Zeitschrift für Physik* **76**, 293 (1932).
- [8] W. H. Barkas, J. N. Dyer, and H. H. Heckman, “Resolution of the Σ^- -mass anomaly”, *Phys. Rev. Lett.* **11**, 26 (1963), <https://link.aps.org/doi/10.1103/PhysRevLett.11.26>.
- [9] F. Bloch, “Zur Bremsung rasch bewegter Teilchen beim Durchgang durch Materie”, *Annalen der Physik* **408**, 285 (1933), <https://onlinelibrary.wiley.com/doi/abs/10.1002/andp.19334080303>.
- [10] W. H. Bragg and R. D. Kleeman, “On the ionization curves of radium”, *Philos Mag.* **S.6**, 726 (1904).
- [11] W. H. Bragg and R. D. Kleeman, “On the alpha particles of radium, and their loss of range in passing through various atoms and molecules”, *Philos Mag.* **S.6**, 318 (1905), <https://archive.org/details/londonedinburghd6101901on/page/318> (visited on 01/24/2019).
- [12] M. Berger, J. Coursey, M. Zucker, and J. Chang, *Stopping-power & range tables for electrons, protons, and helium ions*, Accessed: 2019-01-29, <https://www.nist.gov/pml/stopping-power-range-tables-electrons-protons-and-helium-ions>.

- [13] J. Verburg, “Reducing range uncertainty in proton therapy”, Proefschrift, PhD thesis (Department of Applied Physics, May 2015).
- [14] G. Pausch, J. Petzoldt, M. Berthel, W. Enghardt, F. Fiedler, C. Golnik, F. Hueso-González, R. Lentering, K. Römer, K. Ruhnau, J. Stein, A. Wolf, and T. Kormoll, “Scintillator-based high-throughput fast timing spectroscopy for real-time range verification in particle therapy”, *IEEE Transactions on Nuclear Science* **63**, 664 (2016).
- [15] F. Hueso-González, W. Enghardt, F. Fiedler, C. Golnik, G. Janssens, J. Petzoldt, D. Prieels, M. Priegnitz, K. E. Römer, J. Smeets, F. V. Stappen, A. Wagner, and G. Pausch, “First test of the prompt gamma ray timing method with heterogeneous targets at a clinical proton therapy facility”, *Physics in Medicine and Biology* **60**, 6247 (2015), <https://doi.org/10.1088%2F0031-9155%2F60%2F16%2F6247>.
- [16] J. Berthold, *Single plane compton imaging for range verification in proton therapy - a proof-of-principle study -*, 2018, https://iktp.tu-dresden.de/IKTP/pub/18/Berthold_Masterarbeit.pdf.
- [17] H. Paganetti, “Range uncertainties in proton therapy and the role of Monte Carlo simulations”, *Physics in Medicine & Biology* **57**, R99 (2012), <http://stacks.iop.org/0031-9155/57/i=11/a=R99>.
- [18] F. Hueso-González, F. Fiedler, C. Golnik, T. Kormoll, G. Pausch, J. Petzoldt, K. E. Römer, and W. Enghardt, “Compton camera and prompt gamma ray timing: two methods for in vivo range assessment in proton therapy”, *Frontiers in Oncology* **6**, 80 (2016), <https://www.frontiersin.org/article/10.3389/fonc.2016.00080>.
- [19] J. Smeets, F. Roellinghoff, D. Prieels, F. Stichelbaut, A. Benilov, P. Busca, C. Fiorini, R. Peloso, M. Basilavecchia, T. Frizzi, J. C. Dehaes, and A. Dubus, “Prompt gamma imaging with a slit camera for real-time range control in proton therapy”, *Physics in Medicine and Biology* **57**, 3371 (2012), <https://doi.org/10.1088%2F0031-9155%2F57%2F11%2F3371>.
- [20] J. H. Hubbell and S. M. Seltzer, *X-ray mass attenuation coefficients*, Accessed: 2019-01-29, <https://www.nist.gov/pml/x-ray-mass-attenuation-coefficients>.
- [21] G. F. Knoll, *Radiation detection and measurement*, 4th Edition (John Wiley & Sons, 2010), p. 864.
- [22] B. Kang and J. Kim, “Monte carlo design study of a gamma detector system to locate distal dose falloff in proton therapy”, *IEEE Transactions on Nuclear Science* **56**, 46 (2009).

-
- [23] J. M. Verburg and J. Seco, “Proton range verification through prompt gamma-ray spectroscopy”, *Physics in Medicine and Biology* **59**, 7089 (2014), <https://doi.org/10.1088%2F0031-9155%2F59%2F23%2F7089>.
- [24] E. Sheldon and D. M. Van Patter, “Compound inelastic nucleon and gamma-ray angular distributions for even- and odd-mass nuclei”, *Rev. Mod. Phys.* **38**, 143 (1966), <https://link.aps.org/doi/10.1103/RevModPhys.38.143>.
- [25] J. Kiener, M. Berheide, N. L. Achouri, A. Boughrara, A. Coc, A. Lefebvre, F. de Oliveira Santos, and C. Vieu, “ γ -ray production by inelastic proton scattering on ^{16}O and ^{12}C ”, *Phys. Rev. C* **58**, 2174 (1998), <https://link.aps.org/doi/10.1103/PhysRevC.58.2174>.
- [26] H. Paganetti, *Proton therapy physics* (Taylor & Francis (CRC Press), 2012).
- [27] A.-C. Knopf and A. Lomax, “In vivo proton range verification: a review”, *Physics in Medicine and Biology* **58**, R131 (2013), <https://doi.org/10.1088%2F0031-9155%2F58%2F15%2Fr131>.
- [28] L. Kelleter, A. Wrońska, J. Besuglow, A. Konefał, K. Laihem, J. Leidner, A. Magiera, K. Parodi, K. Rusiecka, A. Stahl, and T. Tessonnier, “Spectroscopic study of prompt-gamma emission for range verification in proton therapy”, *Physica Medica* **34**, 7 (2017), <http://linkinghub.elsevier.com/retrieve/pii/S1120179717300030>.
- [29] B. Kozlovsky, R. J. Murphy, and R. Ramaty, “Nuclear deexcitation gamma-ray lines from accelerated particle interactions”, *The Astrophysical Journal Supplement Series* **141**, 523 (2002), <http://stacks.iop.org/0067-0049/141/i=2/a=523>.
- [30] J. Petzoldt, “Toward the clinical application of the prompt gamma-ray timing method for range verification in proton therapy”, PhD thesis (Technische Universität Dresden, 2016).
- [31] K. Engelmayer, *Messung des Energie-Zeit-Spektrums prompter Gammastrahlung in der Protonenbestrahlung von Kohlenstoff und PMMA*, 2018, https://iktp.tu-dresden.de/IKTP/pub/18/Engelmayer_Kathrin_Bachelorarbeit.pdf.
- [32] J. Llacer, “Positron emission medical measurements with accelerated radioactive ion beams”, *Nuclear Science Applications* **3**, 111 (1988).
- [33] W. Enghardt, P. Crespo, F. Fiedler, R. Hinz, K. Parodi, J. Pawelke, and F. Pönisch, “Charged hadron tumour therapy monitoring by means of PET”, *Nuclear Instruments and Methods in Physics Research Section A: Accelerators, Spectrometers, Detectors and Associated Equipment* **525**, 284 (2004), <http://www.sciencedirect.com/science/article/pii/S0168900204004218>.

- [34] P. C. Lopes, J Bauer, A Salomon, I Rinaldi, V Tabacchini, T Tessonier, P Crespo, K Parodi, and D. R. Schaart, “First in situ TOF-PET study using digital photon counters for proton range verification”, *Physics in Medicine and Biology* **61**, 6203 (2016), <https://doi.org/10.1088%2F0031-9155%2F61%2F16%2F6203>.
- [35] L. Sulak, T. Armstrong, H. Baranger, M. Bregman, M. Levi, D. Mael, J. Strait, T. Bowen, A. E. Pifer, P. A. Polakos, H. Bradner, A. Parvulescu, W. V. Jones, and J. Learned, “Experimental studies of the acoustic signature of proton beams traversing fluid media”, *Nuclear Instruments and Methods* **161**, 203 (1979), <http://www.sciencedirect.com/science/article/pii/0029554X79903860>.
- [36] K. C. Jones, A. Witztum, C. Sehgal, and S Avery, “Proton beam characterization by proton-induced acoustic emission: simulation studies”, *Physics in medicine and biology* **59**, 6549 (2014).
- [37] C.-H. Min, C. H. Kim, M.-Y. Youn, and J.-W. Kim, “Prompt gamma measurements for locating the dose falloff region in the proton therapy”, *Applied Physics Letters* **89**, 183517 (2006), <https://doi.org/10.1063/1.2378561>.
- [38] F. Janssen, G Landry, P. C. Lopes, G Dedes, J Smeets, D. R. Schaart, K Parodi, and F Verhaegen, “Factors influencing the accuracy of beam range estimation in proton therapy using prompt gamma emission”, *Physics in Medicine and Biology* **59**, 4427 (2014), <https://doi.org/10.1088%2F0031-9155%2F59%2F15%2F4427>.
- [39] C. Golnik, F. Hueso-González, A. Müller, P. Dendooven, W. Enghardt, F. Fiedler, T. Kormoll, K. Roemer, J. Petzoldt, A. Wagner, and G. Pausch, “Range assessment in particle therapy based on prompt gamma-ray timing measurements”, *Physics in Medicine and Biology* **59**, 5399 (2014), <https://doi.org/10.1088%2F0031-9155%2F59%2F18%2F5399>.
- [40] S. Agostinelli, J. Allison, K. Amako, J. Apostolakis, H. Araujo, P. Arce, M. Asai, D. Axen, S. Banerjee, G. Barrand, F. Behner, L. Bellagamba, J. Boudreau, L. Broglia, A. Brunengo, H. Burkhardt, S. Chauvie, J. Chuma, R. Chytraccek, G. Cooperman, G. Cosmo, P. Degtyarenko, A. Dell’Acqua, G. Depaola, D. Dietrich, R. Enami, A. Feliciello, C. Ferguson, H. Fesefeldt, G. Folger, F. Foppiano, A. Forti, S. Garelli, S. Giani, R. Giannitrapani, D. Gibin, J. G. Cadenas, I. González, G. G. Abril, G. Greeniaus, W. Greiner, V. Grichine, A. Grossheim, S. Guatelli, P. Gumplinger, R. Hamatsu, K. Hashimoto, H. Hasui, A. Heikkinen, A. Howard, V. Ivanchenko, A. Johnson, F. Jones, J. Kallenbach, N. Kanaya, M. Kawabata, Y. Kawabata, M. Kawaguti, S. Kelner, P. Kent, A. Kimura, T. Kodama, R. Kokoulin, M. Kossov, H. Kurashige, E. Lamanna, T. Lampén, V. Lara, V. Lefebure, F. Lei, M. Liendl, W. Lockman, F. Longo, S. Magni, M. Maire, E. Medernach, K. Minamimoto, P. M. de

- Freitas, Y. Morita, K. Murakami, M. Nagamatu, R. Nartallo, P. Nieminen, T. Nishimura, K. Ohtsubo, M. Okamura, S. O’Neale, Y. Oohata, K. Paech, J. Perl, A. Pfeiffer, M. Pia, F. Ranjard, A. Rybin, S. Sadilov, E. D. Salvo, G. Santin, T. Sasaki, N. Savvas, Y. Sawada, S. Scherer, S. Sei, V. Sirotenko, D. Smith, N. Starkov, H. Stoecker, J. Sulkimo, M. Takahata, S. Tanaka, E. Tcherniaev, E. S. Tehrani, M. Tropeano, P. Truscott, H. Uno, L. Urban, P. Urban, M. Verderi, A. Walkden, W. Wander, H. Weber, J. Wellisch, T. Wenaus, D. Williams, D. Wright, T. Yamada, H. Yoshida, and D. Zschesche, “Geant4—a simulation toolkit”, *Nuclear Instruments and Methods in Physics Research Section A: Accelerators, Spectrometers, Detectors and Associated Equipment* **506**, 250 (2003), <http://www.sciencedirect.com/science/article/pii/S0168900203013688>.
- [41] J. Allison, K. Amako, J. Apostolakis, H. Araujo, P. A. Dubois, M. Asai, G. Barrand, R. Capra, S. Chauvie, R. Chytracsek, G. A. P. Cirrone, G. Cooperman, G. Cosmo, G. Cuttone, G. G. Daquino, M. Donszelmann, M. Dressel, G. Folger, F. Foppiano, J. Generowicz, V. Grichine, S. Guatelli, P. Gumplinger, A. Heikkinen, I. Hrivnacova, A. Howard, S. Incerti, V. Ivanchenko, T. Johnson, F. Jones, T. Koi, R. Kokoulin, M. Kossov, H. Kurashige, V. Lara, S. Larsson, F. Lei, O. Link, F. Longo, M. Maire, A. Mantero, B. Mascialino, I. McLaren, P. M. Lorenzo, K. Minamimoto, K. Murakami, P. Nieminen, L. Pandola, S. Parlati, L. Peralta, J. Perl, A. Pfeiffer, M. G. Pia, A. Ribon, P. Rodrigues, G. Russo, S. Sadilov, G. Santin, T. Sasaki, D. Smith, N. Starkov, S. Tanaka, E. Tcherniaev, B. Tome, A. Trindade, P. Truscott, L. Urban, M. Verderi, A. Walkden, J. P. Wellisch, D. C. Williams, D. Wright, and H. Yoshida, “Geant4 developments and applications”, *IEEE Transactions on Nuclear Science* **53**, 270 (2006).
- [42] *Use cases - reference physics lists*, Accessed: 2019-01-17, <https://geant4.web.cern.ch/node/302>.
- [43] D. Brown, M. Chadwick, R. Capote, A. Kahler, A. Trkov, M. Herman, A. Sonzogni, Y. Danon, A. Carlson, M. Dunn, D. Smith, G. Hale, G. Arbanas, R. Arcilla, C. Bates, B. Beck, B. Becker, F. Brown, R. Casperson, J. Conlin, D. Cullen, M.-A. Descalle, R. Firestone, T. Gaines, K. Guber, A. Hawari, J. Holmes, T. Johnson, T. Kawano, B. Kiedrowski, A. Koning, S. Kopecky, L. Leal, J. Lestone, C. Lubitz, J. M. Damián, C. Mattoon, E. McCutchan, S. Mughabghab, P. Navratil, D. Neudecker, G. Nobre, G. Noguere, M. Paris, M. Pigni, A. Plompen, B. Pritychenko, V. Pronyaev, D. Roubtsov, D. Rochman, P. Romano, P. Schillebeeckx, S. Simakov, M. Sin, I. Sirakov, B. Sleaford, V. Sobes, E. Soukhovitskii, I. Stetcu, P. Talou, I. Thompson, S. van der Marck, L. Welsch-Sherrill, D. Wiarda, M. White, J. Wormald, R. Wright, M. Zerkle, G. Žerovnik, and Y. Zhu, “Endf/b-viii.0: the 8th major release of the nuclear reaction data library with cielo-project cross sections, new standards and thermal scattering

- data”, *Nuclear Data Sheets* **148**, 1 (2018), <http://www.sciencedirect.com/science/article/pii/S0090375218300206>.
- [44] G. Folger, V. N. Ivanchenko, and J. P. Wellisch, “The Binary Cascade”, *The European Physical Journal A - Hadrons and Nuclei* **21**, 407 (2004), <https://doi.org/10.1140/epja/i2003-10219-7>.
- [45] *Geant4 - physics reference manual*, <http://geant4-userdoc.web.cern.ch/geant4-userdoc/UsersGuides/PhysicsReferenceManual/BackupVersions/V10.4/html/index.html> (visited on 01/17/2019).
- [46] K. Roemer, G. Pausch, D. Bemmerer, M. Berthel, A. Dreyer, C. Golnik, F. Hueso-González, T. Kormoll, J. Petzoldt, H. Rohling, P. Thirolf, A. Wagner, L. Wagner, D. Weinberger, and F. Fiedler, “Characterization of scintillator crystals for usage as prompt gamma monitors in particle therapy”, *Journal of Instrumentation* **10**, P10033 (2015), <https://doi.org/10.1088%2F1748-0221%2F10%2F10%2Fp10033>.
- [47] R. Brun and F. Rademakers, “Root – an object oriented data analysis framework”, *Nucl. Instrum. Methods Phys. Res., Sect. A* **389**, 81 (1997), [https://doi.org/10.1016/S0168-9002\(97\)00048-X](https://doi.org/10.1016/S0168-9002(97)00048-X).
- [48] M. Morháč, J. Kliman, V. Matoušek, M. Veselský, and I. Turzo, “Background elimination methods for multidimensional coincidence γ -ray spectra”, *Nucl. Instrum. Methods Phys. Res., Sect. A* **401**, 113 (1997), <http://www.sciencedirect.com/science/article/pii/S0168900297010231>.
- [49] M. Morhac, *ROOT: TSpectrum Class Reference*, <https://root.cern.ch/doc/master/classTSpectrum.html> (visited on 01/14/2019).
- [50] N. D. Gagunashvili, *Comparison of weighted and unweighted histograms*, 2006, http://pos.sissa.it/archive/conferences/050/060/ACAT_060.pdf.
- [51] C. T. J.E. Monahan S. Raboy, “Measurement of the energy of the gamma radiation from neutron capture by hydrogen”, *Nuclear Physics* **24**, 400 (1961), [https://doi.org/10.1016/0029-5582\(61\)90407-2](https://doi.org/10.1016/0029-5582(61)90407-2).
- [52] J. C. Polf, R. Panthi, D. S. Mackin, M. McCleskey, A. Saastamoinen, B. T. Roeder, and S. Beddar, “Measurement of characteristic prompt gamma rays emitted from oxygen and carbon in tissue-equivalent samples during proton beam irradiation”, *Physics in Medicine & Biology* **58**, 5821 (2013), <http://stacks.iop.org/0031-9155/58/i=17/a=5821>.
- [53] F. Hueso-González, M. Rabe, T. A. Ruggieri, T. Bortfeld, and J. M. Verburg, “A full-scale clinical prototype for proton range verification using prompt gamma-ray spectroscopy”, *Physics in Medicine & Biology* **63**, 185019 (2018), <https://doi.org/10.1088%2F1361-6560%2Faad513>.

-
- [54] *PSTAR program*, <https://physics.nist.gov/PhysRefData/Star/Text/PSTAR.html> (visited on 02/13/2019).
- [55] J. Smeets, F. Roellinghoff, D. Prieels, F. Stichelbaut, A. Benilov, P. Busca, C. Fiorini, R. Peloso, M. Basilavecchia, T. Frizzi, J. C. Dehaes, and A. Dubus, “Prompt gamma imaging with a slit camera for real-time range control in proton therapy”, *Physics in Medicine and Biology* **57**, 3371 (2012), <https://doi.org/10.1088%2F0031-9155%2F57%2F11%2F3371>.
- [56] J. Jeyasugiththan and S. W. Peterson, “Evaluation of proton inelastic reaction models in geant4 for prompt gamma production during proton radiotherapy”, *Physics in Medicine & Biology* **60**, 7617 (2015), <http://stacks.iop.org/0031-9155/60/i=19/a=7617>.
- [57] H. P. Wellisch and D. Axen, “Total reaction cross section calculations in proton-nucleus scattering”, *Phys. Rev. C* **54**, 1329 (1996), <https://link.aps.org/doi/10.1103/PhysRevC.54.1329>.
- [58] “Accurate universal parameterization of absorption cross sections III – light systems”, **155**, <http://www.sciencedirect.com/science/article/pii/S0168583X99004796>.

Danksagung

Nach 2343 Tagen neigt sich mein Studium nun dem Ende. Dieser Weg wurde durch zahlreiche Bekanntschaften, Freundschaften und Helfer möglich gemacht. Ich möchte diese Seite dafür nutzen, all diesen Menschen in direkter oder indirekter Form zu danken.

Zuallererst gebührt mein großer Dank Prof. Dr. Arno Straessner, der diese Arbeit ermöglicht und mit unermüdlichem Optimismus begleitet hat und natürlich Dr. Olga Novgorodova, die mich in diesem letzten Jahr betreut hat und die ich immer um Hilfe und Rat fragen konnte. Vielen Dank auch an Prof. Dr. Wolfgang Enghardt für die Übernahme des zweiten Gutachtens.

Danken möchte ich auch den Mitarbeitern im Institut, die organisatorisch und technisch immer geholfen haben, wo sie konnten. Besonderer Dank gilt meinen Bürokollegen, die ich in dieser Zeit hatte: die Menschen aus der K09 und der E16. Dank an Nico Madysa, der mir in Sachen Programmierung immer weiterhelfen konnte. Danke an Johannes Krause für seinen ewigen Optimismus, der mich schon durch die Zeit der Bachelorarbeit begleitet hat und auch nun wieder motivierende Worte fand. Danke auch an Katharina Danziger, die herhalten musste, wenn ich eine Pause von der Arbeit brauchte oder jemanden, der mir Rat zu Bildern in \LaTeX gab.

Weiterhin gilt mein Dank all den Korrekturlesern: Maximilian Hils, der in einem frühen Stadium der Arbeit erste wichtige und gute Hinweise geben konnte, Tim Kaltoven und Kevin Krechan, die immer ein offenes Ohr für Fragen hatten und María González Torres. Dank an Jenny Morzik und Anna Bakker, die versuchten, meine englische Rechtschreibung und Grammatik in Form zu bringen.

Natürlich möchte ich auch meinen Wegbegleitern im FSR und der restlichen studentischen Selbstverwaltung danken. Ihr habt das Studium zu einem unvergleichlichen Erlebnis gemacht und dazu beigetragen, dass ich mich weniger oft auf das Studium konzentriert habe.

Ich danke meiner WG für die schöne gemeinsame Zeit, die guten Gespräche und das gute Essen. Ihr habt mir die nicht immer ganz einfache Zeit der Masterarbeit in vielen Momenten ein Stückchen erleichtert.

Vielen Dank an Annika Schlögl, ohne die ich das Physik-Studium wohl nach dem Bachelor aufgegeben hätte und die mich durch alle Zeiten, ob gut oder schlecht, begleitet hat und die immer für mich da ist.

Auch möchte ich meiner Familie danken, auf die ich immer zählen kann und durch die das Studium ohne starken äußeren Druck ablaufen konnte.

Zuletzt möchte ich Liane Dröbner danken, die dieses letztes Jahr zu etwas ganz Besonderem gemacht hat. Danke für deine Unterstützung und Liebe! Ohne dich wäre das letzte Jahr nie so schön geworden. Eine schönere Begleitung zum letzten Studienjahr konnte ich mir nicht wünschen. Danke!

Selbstständigkeitserklärung

Hiermit erkläre ich, dass ich diese Arbeit im Rahmen der Betreuung am Institut für Kern- und Teilchenphysik der TU Dresden ohne unzulässige Hilfe Dritter verfasst und alle Quellen als solche gekennzeichnet habe.

Marius Walther
Dresden, 01. März 2019